NOVEL METHODS FOR SAR IMAGING PROBLEMS

A DISSERTATION SUBMITTED TO
THE DEPARTMENT OF ELECTRICAL AND ELECTRONICS ENGINEERING
AND THE GRADUATE SCHOOL OF ENGINEERING AND SCIENCE
OF BILKENT UNIVERSITY
IN PARTIAL FULFILLMENT OF THE REQUIREMENTS
FOR THE DEGREE OF
DOCTOR OF PHILOSOPHY

By
Salih Uğur
June, 2013

I certify that I have read this thesis and that in my opinion it is fully adequate, in scope and in quality, as a dissertation for the degree of Doctor of Philosophy.

Prof. Dr. Orhan Arıkan (Advisor)

I certify that I have read this thesis and that in my opinion it is fully adequate, in scope and in quality, as a dissertation for the degree of Doctor of Philosophy.

Assoc. Prof. Dr. Sinan Gezici

I certify that I have read this thesis and that in my opinion it is fully adequate, in scope and in quality, as a dissertation for the degree of Doctor of Philosophy.

Assoc. Prof. Dr. Uğur Güdükbay

I certify that I have read this thesis and that in my opinion it is fully adequate, in scope and in quality, as a dissertation for the degree of Doctor of Philosophy.

Prof. Dr. Enis Çetin

I certify that I have read this thesis and that in my opinion it is fully adequate, in scope and in quality, as a dissertation for the degree of Doctor of Philosophy.

Assoc. Prof. Dr. Ali Cafer Gürbüz

Approved for the Graduate School of Engineering and Science:

Prof. Dr. Levent Onural
Director of the Graduate School

ABSTRACT

NOVEL METHODS FOR SAR IMAGING PROBLEMS

Salih Uğur
Ph.D. in Electrical and Electronics Engineering
Supervisor: Prof. Dr. Orhan Arıkan
June, 2013

Synthetic Aperture Radar (SAR) provides high resolution images of terrain reflectivity. SAR systems are indispensable in many remote sensing applications. High resolution imaging of terrain requires precise position information of the radar platform on its flight path. In target detection and identification applications, imaging of sparse reflectivity scenes is a requirement. In this thesis, novel SAR image reconstruction techniques for sparse target scenes are developed. These techniques differ from earlier approaches in their ability of simultaneous image reconstruction and motion compensation. It is shown that if the residual phase error after INS/GPS corrected platform motion is captured in the signal model, then the optimal autofocused image formation can be formulated as a sparse reconstruction problem. In the first proposed technique, Non-Linear Conjugate Gradient Descent algorithm is used to obtain the optimum reconstruction. To increase robustness in the reconstruction, Total Variation penalty is introduced into the cost function of the optimization. To reduce the rate of A/D conversion and memory requirements, a specific under sampling pattern is introduced. In the second proposed technique, Expectation Maximization Based Matching Pursuit (EMMP) algorithm is utilized to obtain the optimum sparse SAR reconstruction. EMMP algorithm is greedy and computationally less complex resulting in fast SAR image reconstructions. Based on a variety of metrics, performances of the proposed techniques are compared. It is observed that the EMMP algorithm has an additional advantage of reconstructing off-grid targets by perturbing on-grid basis vectors on a finer grid.

Keywords: Synthetic Aperture Radar, Phase Error Correction, Compressed Sensing, Total Variation, Expectation Maximization Based Matching Pursuit.

ÖZET

SAR GÖRÜNTÜLEME PROBLEMLERİ İÇİN YENİ METODLAR

Salih Uğur
Elektrik Elektronik Mühendisliği, Doktora
Tez Yöneticisi: Prof. Dr. Orhan Arıkan
Haziran, 2013

Sentetik Açıklıklı Radar (SAR) yüzey yansımasının yüksek çözünürlüklü görüntüsünü sağlar. SAR sistemleri pek çok uzaktan algılama uygulamasının vazgeçilmezi olmuştur. Yüzeyin yüksek çözünürlüklü görüntülenmesi radar platformu uçuş rotasının hassas pozisyon bilgisini gerektirir. Hedef tespit ve tanımlama uygulamalarında seyrek yansıtıcı yüzeylerin görüntülenmesi gerekir. Bu tezde, seyrek hedef yüzeyleri için yeni SAR görüntü geriçatımı teknikleri geliştirilmiştir. Bu teknikler daha öncekilerden, görüntü oluşturulması ve platform hareket hatalarının giderilmesi işlemlerinin eş zamanlı yapılmaları açısından farklılaşmaktadır. Platform hareketinin INS/GPS yardımıyla düzeltilmesi sonrası kalan faz bozukluğunun sinyal modeline katılmasıyla, en iyi otomatik odaklanmış görüntü oluşturulması işlemi bir seyrek geri çatım problemi olarak ortaya konulmaktadır. İlk önerilen teknikte, eniyi geri çatımı elde etmek için Doğrusal Olmayan Eşlenik Bayır Küçülme algoritması kullanılmaktadır. Geriçatımın gürbüzlüğünün arttırılması amacıyla Toplam Değişim cezası da eniyilemenin maliyet fonksiyonuna eklenmiştir. Analog/sayısal çeviricilerinin hız ve hafıza gereksinimlerini düşürebilmek amacıyla özel bir alt örnekleme yapısı geliştirilmiştir. Önerilen ikinci teknik, eniyi seyrek SAR görüntü geriçatımı için Enbüyültümü Tabanlı Uyumlama Takibi algoritmasını kullanmaktadır. Enbüyültümü Tabanlı Uyumlama Takibi algoritması fırsatçı bir algoritma olup daha az hesaplama karmaşıklığı içermektedir ve bu sayede hızlı SAR görüntü geri çatımına olanak vermektedir. Önerilen tekniklerin performansları muhtelif performans parametreleri baz alınarak karşılaştırılmıştır. Enbüyültümü Tabanlı Uyumlama Takibi algoritmasının ek bir avantajı küçük değişikliklerle ızgara üzerinde olmayan hedeflerin geri çatımına da olanak vermesidir.

Anahtar sözcükler: Sentetik Açıklıklı Radar, Faz Hatası Düzeltimi, Sıkıştırılmış Algılama, Toplam Değişim, Beklenti Enbüyültümü Tabanlı Uyumlama Takibi.

Acknowledgement

First of all, I would like to thank my advisor, Prof. Dr. Orhan Arıkan whose guidance has made it possible to write this doctoral thesis. His unconditional help and support encouraged me to start, continue, and finish my research twelve years after from leaving university.

I would like to thank members of the thesis monitoring committee, Assoc. Prof. Dr. Sinan Gezici and Assoc. Prof. Dr. Selim Aksoy for their insightful discussions and suggestions. Besides, I would like to thank my Ph. D. thesis defense jury members, Assoc. Prof. Dr. Uğur Güdükbay, Prof. Dr. Enis Çetin, and Assoc. Prof. Dr. Ali Cafer Gürbüz for carefully reviewing and commenting on my thesis.

I would also like to thank my parents to whom I owe everything. I appreciate indulgence of my beloved daughter Dilara and son Ömer towards their ever-busy father.

Finaly, I would like to thank my wife Deniz for her support and patience during all my studies.

Contents

List of Figures

List of Tables

Chapter 1

Introduction

Synthetic Aperture Radar (SAR) systems provide high resolution images of terrain reflectivity. Typically, an airborne or spaceborne platform carries a monostatic radar system on a straight flight path, while the radar transmits and receives echoes from the area of interest. The received and digitized radar returns are coherently processed to obtain significantly higher resolutions in azimuth direction that could have been obtained by a large aperture antenna.

SAR systems are widely used in ground surveillance, terrain mapping and environmental monitoring applications due to their ability to provide high resolution images. They have wide range of users from commercial, scientific, and military fields. Commercial users focus on the manage and monitor the Earth's resources while scientific users has a much wider range from monitoring global climate change to discovering leakage detection on the sea. In military applications, SAR is primarily used in intelligence, surveillance and reconnaissance (ISR) missions. Increased demand on high precision ISR outputs requires sub-meter or even higher resolutions from SAR images. High resolution SAR systems are becoming competitive alternatives and supplements of Electro-Optic/Infrared (EO/IR) cameras for ISR applications. Also, capability of operating in all weather conditions makes them very appealing for surveillance applications where performance of EO/IR cameras heavily depend on the atmospheric conditions and time of the day.

In a typical digital SAR image reconstruction processing chain, the received analog signal is first down-converted and sampled by using an A/D converter operating above the Nyquist rate of sampling (Figure 1.1). The sampling rate of

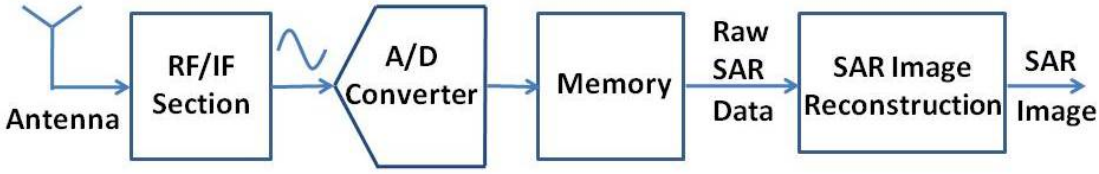

Figure 1.1: Typical SAR image formation process.

the A/D converter depends on the bandwidth of the SAR system which determines the range resolution. The A/D converted signal is written in a memory for further processing. The size of the required memory is derived from the data rate of the A/D converter and the processing power of the SAR image formation processor. The stored data is either processed in real-time by an on-board processor or transferred by a data link to a ground station where the image formation takes place.

SAR range resolution depends on the bandwidth of the transmitted signal similar to classical radars. High bandwidth results finer resolution. Azimuth resolution in SAR depends on the synthetic aperture length. Longer aperture provides finer azimuth resolution.

SAR has two main modes, namely stripmap and spotlight. In stripmap mode SAR (Figure 1.2), the radar antenna angle with respect to platform route is held constant. It gives the strip image of larger scenes in coarser resolutions. In spotlight mode SAR (Figure 1.3), the radar antenna is directed to a constant position in the imaged scene throughout the data collection phase. In this mode finer resolutions are obtained for relatively small scenes. In military ISR applications, typical SAR mission flow is as follows: First a stripmap mode image of the scanned area is examined usually with the help of a computer to detect possible targets. For detected ones, a spotlight mode mission is performed to obtain high resolution images of the targets. The SAR image reconstruction requires to collect all the data corresponding to the synthetic aperture. In other

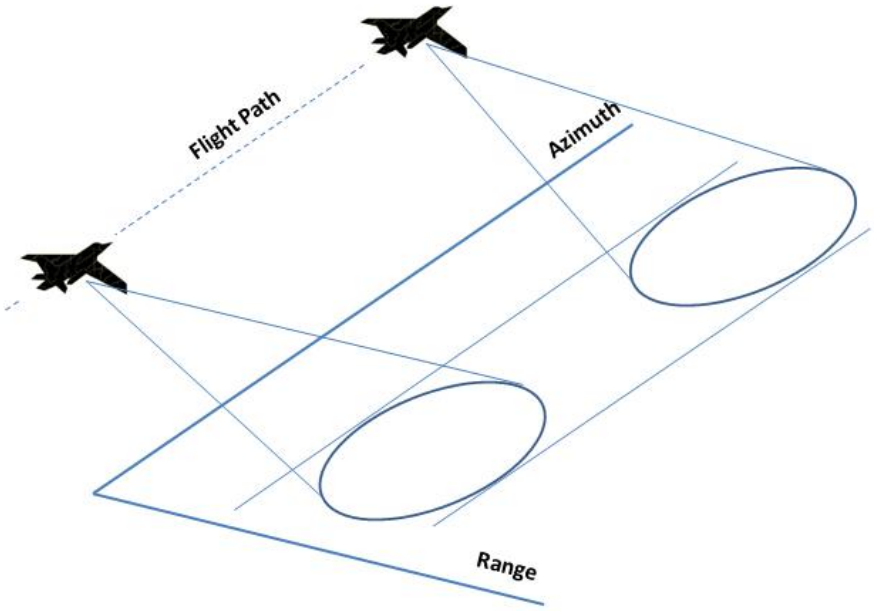

Figure 1.2: Strip mode SAR geometry.

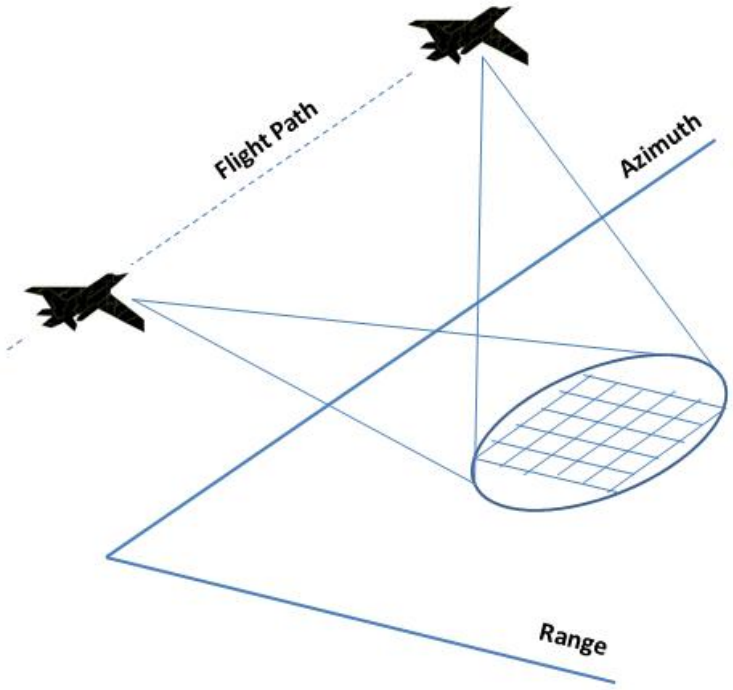

Figure 1.3: Spot mode SAR geometry.

words, reconstruction process waits for the SAR to collect all the data for the corresponding image. Therefore there is a lag between the data collection and reconstruction times of the SAR image. Due to this lag, SAR image reconstruction is called as a near-real time process.

Apart form the data collection geometry, SAR modes mainly differ by their respective reconstruction algorithms. A variety of different reconstruction algorithms have been proposed for both modes of operation. For stripmap mode, range-Doppler [1, 2, 3], chirp scaling [4], and $w - K$ [5] algorithms are commonly used techniques. Main feature of range-Doppler algorithm is to perform all operations in one dimension at a time. Chirp scaling algorithm eliminates the interpolator used for range cell migration correction in range-Doppler algorithm. $w - K$ algorithm corrects range and azimuth frequency dependence of azimuth range coupling in two dimensional frequency domain. Polar Format Algorithm (PFA) [6] and Filtered Back Projection (FBP) [7, 8] are the algorithms that are widely used in spotlight mode image reconstruction. PFA utilizes the fact that de-ramped SAR phase history signal is the Fourier transformation of the reflectivity of the scene to be imaged. FBP, originated from computer aided tomography, reconstructs SAR image by back propagating received signals collected through the synthetic aperture to imaged scene.

1.1 SAR Data Acquisition

In this part, we will first focus on the characteristics of the SAR data acquisition in spotlight mode operation. Although they can be applied to other modes of operation, our methods, especially the ones using Compresses Sensing (CS) techniques assume the SAR is in spotlight mode for the sake of brevity originating from the basic Fourier transform relation between the received signal and the ground reflectance.

In spotlight mode SAR, at regular intervals along the flight path, the radar transmits the real part of a linear frequency modulated (FM) chirp waveform

$s(t)$, which is defined as:

$$s(t) = \begin{cases} e^{j(\omega_0 t + at^2)}, & |t| \leq \frac{T}{2} \\ 0, & \text{otherwise} \end{cases} \tag{1.1}$$

where ω_0 is the RF carrier frequency in radians, $2a$ is the FM rate and T is the pulse duration. At each look angle, θ, which corresponds to a different azimuth

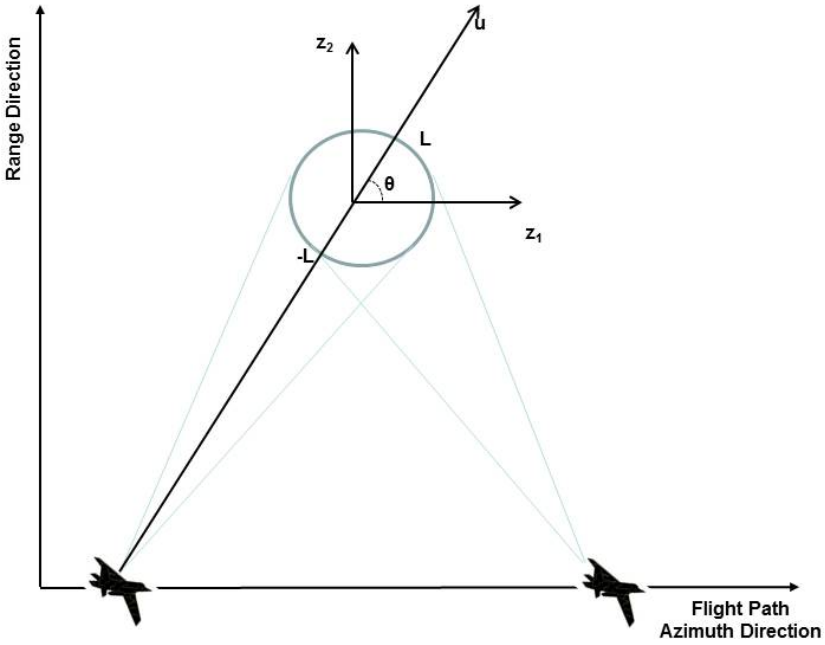

Figure 1.4: Spotlight mode SAR imaging geometry.

position along the synthetic aperture (see Figure 1.4), the relation between the received and demodulated signal $y_\theta(t)$, and the scene reflectivity $x(z_1, z_2)$ can be expressed as [6],

$$y_\theta(t) = \iint_{\sqrt{z_1^2+z_2^2} \leq L} x(z_1, z_2) \exp\{-j\Omega(t)(z_1 \cos(\theta) + z_2 \sin(\theta))\} dz_1 dz_2 \tag{1.2}$$

where L is the spatial extent of the ground patch and

$$\Omega(t) = (2/c)(\omega_0 + 2a(t - (2R_\theta/c))), \tag{1.3}$$

is the radial spatial frequency. R_θ in $\Omega(t)$ formulation corresponds to distance between the platform and the imaged target scene center at a look angle θ. The demodulated signal $y_\theta(t)$ can also be written as the band-pass filtered Fourier transform of the projection of the ground reflectivity $x(z_1, z_2)$ at the angle θ, by using the projection slice theorem [7]:

$$y_\theta(t) = \int_{-L}^{L} q_\theta(u) \exp\{-j\Omega(t)u\} du, \tag{1.4}$$

where u is the axis from the platform to the center of the imaged area at the angle θ, and $q_\theta(u)$ is the projection of the scene reflectivity $x(z_1, z_2)$ at the angle θ, given by;

$$q_\theta(u) = \iint \delta(u - z_1\cos(\theta) - z_2\sin(\theta)) x(z_1, z_2) dz_1 dz_2, \tag{1.5}$$

and is called the range profile [9]. Matrix based formulation of the spotlight mode SAR image reconstruction problem can be written by discretizing the integral in Eq. 1.2 using its uniform Riemann sum approximation [10]:

$$\mathbf{y}_\theta \;=\; \mathbf{G}_\theta\, \mathbf{x}, \tag{1.6}$$

where, $\mathbf{x}$ and $\mathbf{y}_\theta$ are vectorized forms of the 2-D ground reflectivity distribution and the demodulated received signal, respectively. The vectorized form of $\mathbf{x}$ is obtained by stacking the columns of the 2-D ground reflectivity distribution matrix and the vectorized form of $\mathbf{y}_\theta$ corresponds to the fast-time samples taken at the look angle θ. Finally, $\mathbf{G}_\theta$ is the complex valued discrete SAR projection operator at the angle θ relating the received signal to the unknown reflectivities.

The received signal at each azimuth position is sampled by an A/D converter. All the signals received along the synthetic aperture can be written in a vector form by stacking their respective signal samples. This is achieved by appending the range bins taken from an azimuth location to the bins taken from the next azimuth location. The discretized reflectivity matrix can also be written in a vector form by stacking its respective columns. The relation between the received signal vector and the reflectivity vector then can be written as [9],

$$\mathbf{y} = \mathbf{G}\,\mathbf{x} + \mathbf{w}, \tag{1.7}$$

where $\mathbf{y}$ is the received signal (the measurement vector), $\mathbf{G}$ is the complex valued discrete SAR projection operator matrix (composed of all $\mathbf{G}_\theta$ throughout the synthetic aperture), $\mathbf{x}$ is the reflectivity vector and $\mathbf{w}$ is the additive complex white Gaussian measurement noise vector. Assuming N azimuth and N range points results $N \times N$ rectangular grid for SAR image. This image has total number of $m = N \times N$ pixels. Then, $\mathbf{y}, \mathbf{x}$, and $\mathbf{w}$ are $m \times 1$ vectors. $\mathbf{G}$ is a matrix with size $m \times m$.

1.2 Phase Error Due To Platform Motion in SAR

SAR systems need accurate distance and angle information between the SAR platform and the reference point in the terrain of interest in order to establish the synthetic aperture precisely. However, especially in airborne SAR applications, due to the limited accuracy of the navigational sensors, there is always some residual error left in the estimation of the actual flight path. These uncompensated platform motion errors cause uncertainties in distance and angle measurements which result in phase errors in the received SAR signal. Let δR represents this measurement error which results mixing error and causes phase errors in the received signal. Hence the demodulation output of Eq. 1.4 becomes [11]:

$$y_{\theta p}(t) = e^{j\delta R\,\Omega(t)} \int_{-L}^{L} q_\theta(u) \exp\{-j\Omega(t)u\} du = e^{j\phi(t)}\, y_\theta(t), \tag{1.8}$$

where $y_{\theta p}(t)$ is the received signal with phase error due to an error of δR in the platform position from the scene center. Since $\Omega(t) = (2/c)(\omega_0 + 2a(t - (2R_\theta/c)))$, the phase error term $\phi(t)$, has a constant part and a time varying part. Following Eq. 1.8, the exponential multiplication of the phase error can be inserted to the signal model and the measurement relation of Eq. 1.7 becomes:

$$\mathbf{y_p} = \mathbf{\Phi}\, \mathbf{y} = \mathbf{\Phi}\, \mathbf{G}\, \mathbf{x} + \mathbf{w}, \tag{1.9}$$

Here, $\mathbf{\Phi}$ is a diagonal matrix representing phase errors for every measurement taken from the imaged scene and is given below,

$$\mathbf{\Phi} = \begin{pmatrix} e^{j\phi_1} & & & \\ & e^{j\phi_2} & & \\ & & \ddots & \\ & & & e^{j\phi_m} \end{pmatrix}. \tag{1.10}$$

Here m is the total number of measurements and ϕ_i's are the phase errors in radians incurred at the i^{th} measurement bin. The error in the range compressed data due to phase error is generally ignored, because the resultant range error is typically a small fraction of a range resolution bin [11]. Therefore, phase errors do not depend on the range axis and they are assumed to be the same for all the data corresponding to an azimuth point,

$$\begin{pmatrix} y_{p_1} \\ y_{p_2} \\ \vdots \\ y_{p_N} \end{pmatrix} = \begin{pmatrix} e^{j\phi_1} & & & \\ & e^{j\phi_2} & & \\ & & \ddots & \\ & & & e^{j\phi_N} \end{pmatrix} \begin{pmatrix} G_1 \\ G_2 \\ \vdots \\ G_N \end{pmatrix} \mathbf{x} + \mathbf{w}, \tag{1.11}$$

where y_{p_i} is the partition of the measurement vector y_p which contains all the range points corresponding to the azimuth point i, ϕ_i is the phase error at the azimuth point i, G_i is the partition of the matrix G corresponding to the range bins of the azimuth point i and N is the total number of azimuth points. From now on, G_i is used instead of G_θ for representing matrix partition of G in order not to confuse with angle.

Phase errors are the main cause of degradations in high resolution SAR images limiting achievable performance especially in the azimuth direction. These errors, depending on their nature, can cause geometric distortions, loss of resolution/contrast, decrease in SNR and even generate spurious targets [6]. An example of a SAR image distorted by phase error is given in Figure 1.5.b. The synthetically generated original image is presented in Figure 1.5.a. Both of these images are reconstructed by PFA. Figure 1.5.c gives the phase error in radians added to the original image.

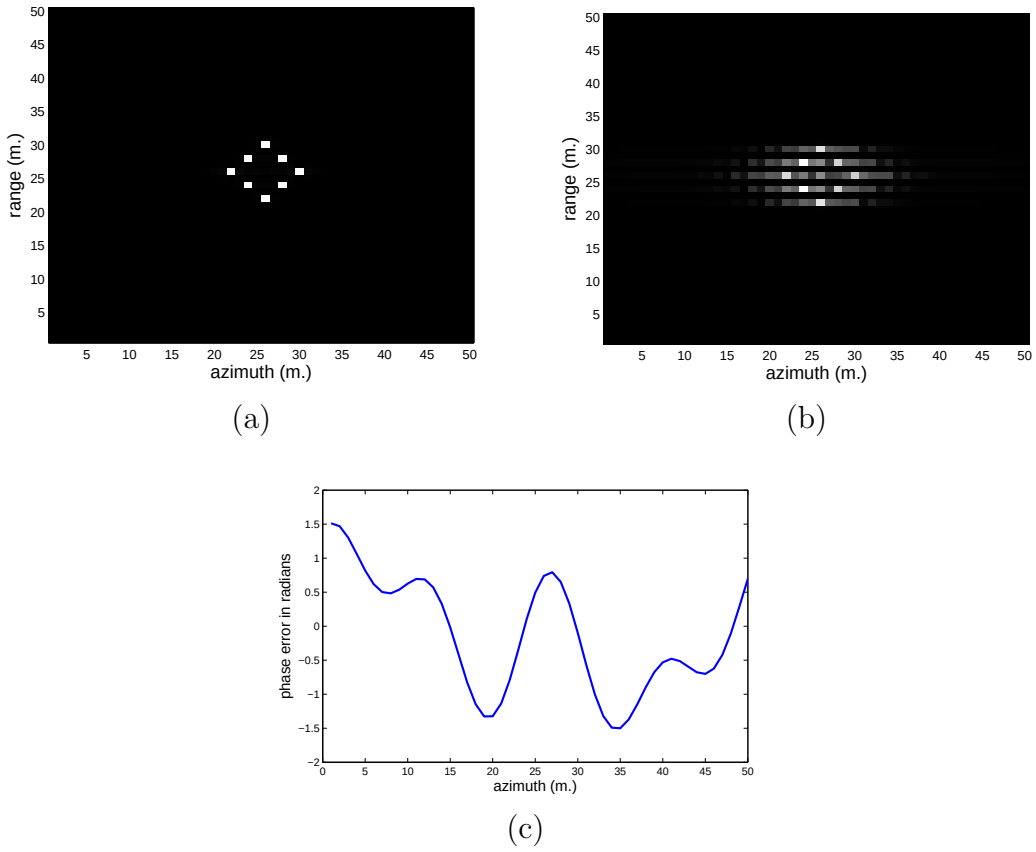

Figure 1.5: (a) Synthetically generated SAR image. (b) SAR image with phase error. (c) Added phase error in radians.

Modern SAR systems have high range and azimuth resolutions which necessitate large bandwidths even in excess of $500MHz$. These systems typically requires higher operational frequencies because of the desired bandwidths in the RF and antenna subsystems. Higher operational frequencies increase the required accuracy levels of motion compensation techniques. If not compensated, these motion errors cause greater amount of phase errors at higher frequencies. As a result, higher operational frequencies create significant challenges for autofocus techniques. Furthermore, classical image reconstruction techniques for higher frequency SAR systems require full band, fast A/D converters to digitize the received signal resulting in larger onboard storage systems. In addition, if the raw data is to be transmitted to another platform for processing, transmission of full band data requires more time or bandwidth.

1.3 SAR Motion Compensation by Phase Gradient Autofocus Technique

SAR platforms are generally equipped with an Inertial Measurement Unit (IMU) to estimate their actual track which can have considerable difference than the planned one. Even when the IMU is used, there is an error left in the estimation of the actual track which causes a phase error in the SAR signal. Autofocus algorithms are image restoration techniques which can be applied to overcome the degradations related to phase errors. There are several autofocus techniques [6, 12, 13, 14, 15, 16, 17, 18, 19, 20] to estimate and correct phase errors by using dedicated algorithms on raw SAR data. These algorithms can be applied to a wide range of SAR images successfully. Once a reliable estimate for the phase error is available, the raw SAR data is corrected to obtain highly improved reconstructions. The autofocus problem is still an active research area in SAR community. The main difficulty in autofocus problem is the nonlinear coupling between the unknown target scene reflectances and the phase error. Recently proposed modern autofocus techniques apply algorithms based on a bilinear parametric model via semidefinite relaxation [21, 22] and claim improved performances over existing

methods.

Phase Gradient Autofocus (PGA) algorithm [18] is a widely used technique to compensate phase error in SAR images. It is a non-parametric estimator and its basic algorithmic steps are given in Figure 1.6[11]. PGA first center shifts

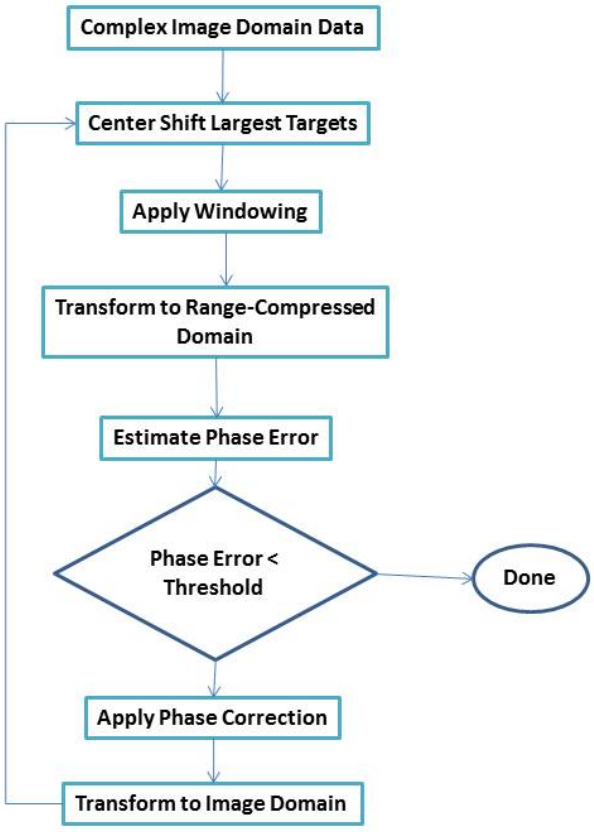

Figure 1.6: PGA algorithm: PGA is applied to complex valued image data. It finds and center shifts the most powerful scatterers in each range bin. After applying windowing and transforming the data to range compressed domain, PGA estimates the phase error. These steps are repeated for a fixed number of times or until a certain threshold is reached.

the brightest pixels on the complex image in each range bin. Then, it applies windowing to suppress the effects of other targets residing in the same range bin. PGA estimates the phase error in the range compressed domain. Then, it applies phase correction using its estimate. These steps are iterated until there is negligible difference between iterations at which point the phase error estimate

is obtained. Usually, around three iterations of the PGA is sufficient to estimate phase errors. The PGA algorithm is applied to the phase error distorted image

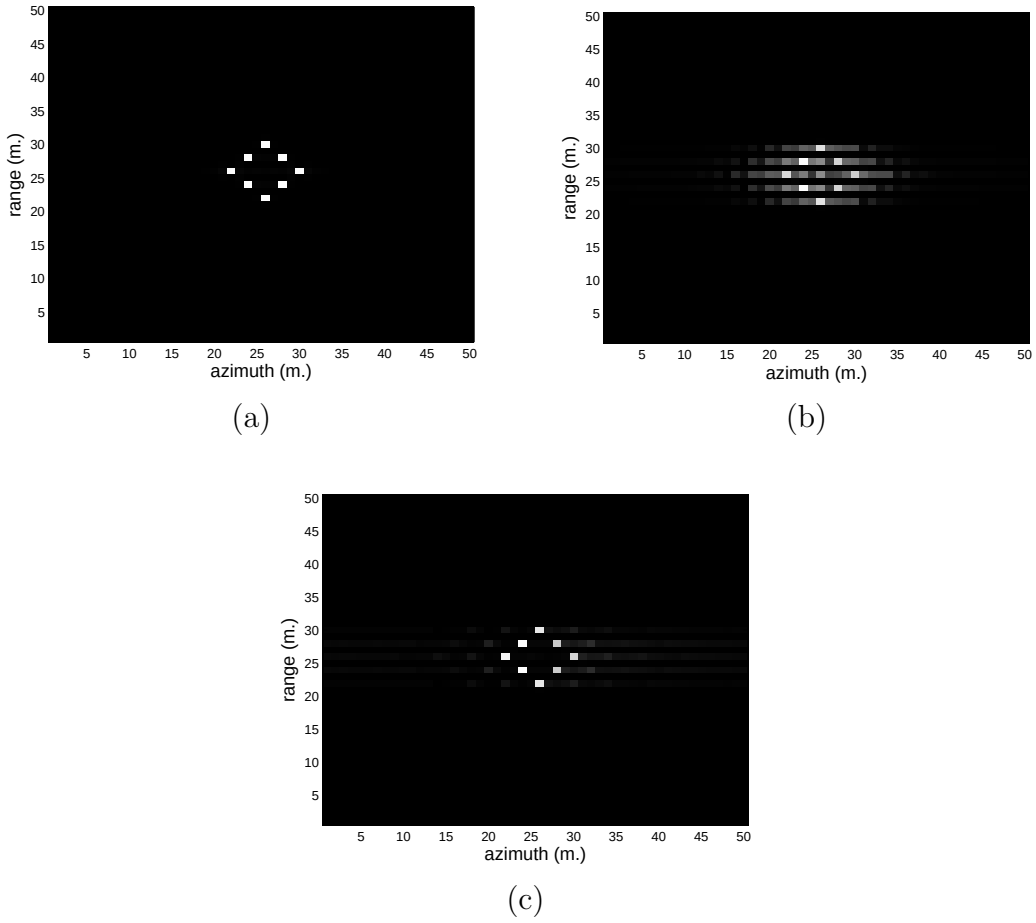

Figure 1.7: (a) Original SAR image. (b) SAR image with phase error. (c) SAR image reconstructed by PFA and autofocused by using PGA technique.

of Figure 1.5.b and the resultant image is given in Figure 1.7.c.

Chapter 2

SAR Image Reconstruction and Autofocus by Compressed Sensing

Recent developments in Compressed Sensing (CS) techniques have an impact on the SAR image reconstruction as well. Unlike classical SAR image processing techniques, CS methods can operate on downsampled data to reconstruct SAR images where targets of interest are sparse in a certain transform domain. CS SAR image reconstruction techniques proposed in the literature model the image forming process as a sparse inverse reconstruction problem. In [23, 24], the inverse problem is formulated as a convex l_1 norm minimization and its solution is obtained by linear programming or approximated by greedy pursuit algorithms. The l_1 norm minimization term in the cost function of the convex minimization problem enforces sparsity. A similar approach is also used in [25] for sparse reconstruction of SAR images which uses the basis pursuit algorithm for the solution of the problem and demonstrates the super resolution property. Several computational tools are available in the literature [26, 27] which can be applied to l_1 norm minimization problems. In [10], the cost function with l_1 term is solved by finding roots on the Pareto curve [26]. But they also modify the reconstruction problem by adding a total variation penalty into the cost function to reduce the speckle

noise effects, which requires development of a dedicated solver. In Fourier imaging applications, the effect of p-norm regularization under amplitude and phase errors is studied in [28], where it is stated that for $p < 2$ gradient descent optimizations reduce amplitude and phase irregularities. In [29] phase errors are accounted as SAR observation model errors and an iterative sparsity-driven method for simultaneous SAR imaging and autofocus is proposed. A coordinate descent technique is used to minimize the cost function. This method uses the fully sampled raw data to reconstruct the SAR image. Similarly, joint formulation of SAR reconstruction and autofocus has been proposed in [30], where only 50% of the Nyquist rate samples are used for the processing. There are also several other sparse SAR image reconstruction algorithms that are recently reviewed and compared in [31].

In this chapter, a new CS based sparse SAR image reconstruction technique is proposed. The proposed technique also performs autofocus enabling simultaneous image reconstruction and correction of phase errors. The proposed technique models the phase error as part of the data acquisition and then employs a CS based approach for image reconstruction and optimal phase error correction. The non-linear conjugate gradient descent algorithm is used to minimize the cost function. In addition to phase error correction, the proposed technique also incorporates total variation (TV) penalty into the cost function, hence it is called as the CS-PE-TV technique. Typical CS applications rely on l_1 norm minimization approaches. However, adding TV penalty into the cost function of the SAR image reconstruction improves the quality of the reconstruction by suppressing intensity variations caused by speckle noise, without a smoothing effect on the boundaries [10]. As a novel way of integrating both TV penalty and phase error into the cost function of the sparse SAR image reconstruction problem, the proposed technique improves the overall reconstruction quality.

To facilitate practical implementation, a new under-sampling methodology is presented in this study. It reduces the A/D conversion rate to obtain the required samples for CS SAR image reconstruction, allowing us to overcome the hardware limitations of wide band SAR applications.

2.1 Compressed Sensing: A Short Review

Compressed sensing (CS) is a relatively new signal processing technique [32, 33]. It can provide reliable reconstruction of a signal from a set of linear underdetermined measurements. In order to apply CS, the signal should have a sparse representation in a known basis. Since sparsity is encountered in many natural signals, CS has found diverse applications. Consider the following linear measurement model:

$$\mathbf{y} = \mathbf{G}\,\mathbf{x}, \tag{2.1}$$

where $\mathbf{G}$ is the measurement matrix, $\mathbf{y}$ is the measured signal and $\mathbf{x}$ is the unknown signal which can be represented sparsely in a known basis:

$$\mathbf{x} = \mathbf{\Psi}\,\alpha, \tag{2.2}$$

where columns of $\mathbf{\Psi}$ are basis vectors and α is the vector of sparse representation coefficients. Then Eq. 2.1 can be written as,

$$\mathbf{y} = \mathbf{A}\,\alpha, \tag{2.3}$$

where $\mathbf{A} = \mathbf{G}\,\mathbf{\Psi}$. The sparse solution for the linear model of Eq. 2.1 is found by solving the following l_0 norm minimization problem,

$$\min \|\alpha\|_0 \qquad \textit{such that} \qquad \mathbf{y} = \mathbf{A}\,\alpha, \tag{2.4}$$

where $\|\alpha\|_0$ describes the l_0 norm which is the number of non-zero entries in α. The solution to the problem in Eq. 2.4 is combinatorial in nature with prohibitive computational load in practical applications. Convex relaxation of the l_0 problem to the following l_1 problem,

$$\min \|\alpha\|_1 \qquad \textit{such that} \qquad \mathbf{y} = \mathbf{A}\,\alpha, \tag{2.5}$$

enables use of efficient solution techniques and programming tools for its solution [34, 35, 36, 37, 38, 39, 40, 41]. Commonly used sparse reconstruction algorithms are claimed as second order cone programming (SOCP), gradient descent approaches, greedy search algorithms, weighted least squares and Bregman iterations.

Uniqueness of the sparse solution of Eq. 2.4 is guaranteed when $spark(\mathbf{A})/2 \geq \|\alpha\|_0$ is satisfied [42], where *spark* of a matrix $\mathbf{A}$ is defined as the size of the smallest linearly dependent column subset. The $spark(\mathbf{A})$ not only controls uniqueness in Eq. 2.4 but also controls it in Eq. 2.5. No sparsity bound implies the equivalence of Eqs. 2.4 and 2.5 unless $spark(\mathbf{A})/2 \geq \|\alpha\|_0$. A stronger condition than the spark of a matrix is the Restricted Isometry Property (RIP), which is defined as,

$$(1-\delta_s)\|\alpha\|_2 \;\leq\; \|\mathbf{A}\alpha\|_2 \;\leq\; (1+\delta_s)\|\alpha\|_2 \qquad (2.6)$$
$$such\ that \quad \delta_s > 0,\ \|\alpha\|_0 < s,$$

where isometry constant δ_s satisfies, $0 \leq \delta_s < 1$ [43]. RIP provides an upper bound for the sparsity of a signal so that its energy is preserved by a given amount through the transformation by the operator. It is proven that Eqs. 2.4 and 2.5 provide the same solution if α is sparse and $\mathbf{A}$ holds RIP [43, 44]. Unfortunately, even for moderate dimensional operators, finding RIP of a given operator is computationally impractical. However, a few classes of matrices are shown to posses RIP almost certainly [33, 43, 44] which include random matrices with independent identically distributed entries, Fourier ensemble matrices, and general orthogonal measurement ensembles. Note that the general orthogonal measurement ensembles can be generated by randomly selecting n rows from $m \times m$ orthonormal matrix and re-normalizing the columns [43].

Application of CS techniques has increased dramatically since its mathematical foundations were laid in 2006 [32, 33]. Medical and electro-optic imaging applications benefit significantly from CS techniques due to the well known bases that are used for sparse representation of the imaged scenes [45]. Applications of CS to radar and SAR are also investigated [23, 24, 25, 10, 31, 46, 47, 48, 49]. The main difficulty in applying CS to SAR imaging is finding an appropriate basis for the sparse representation of SAR images. Due to their speckle noise content, SAR images of terrain cannot be sparsely represented in known domains. Speckle noise is caused by the coherent contributions of multiple distributed reflecting objects in a resolution cell [50]; it creates difficulties in finding sparse basis for SAR images. However, for radar scenes with highly reflective man-made objects, either wavelet or standard basis vectors can be chosen for the sparse representation of

the scene reflectivity distribution [51]. Hence, CS techniques can be applied to SAR image reconstructions of target scenes containing highly reflective objects.

2.2 SAR Raw Data Sampling Technique for Compressed Sensing Applications

CS techniques recover an S-sparse signal of length N with high probability if the measurement matrix satisfies RIP and the number of measurements are greater than $O(S\log(N/S))$ [52]. Reconstructing a sparse signal with fewer measurements than its corresponding Nyquist rate helps reduce the sampling rate and the amount of raw data to be processed. Reduced sampling rates allow usage of slower A/D converters in SAR systems. Furthermore the reduced amount of raw data reduces the memory requirements of the system and the necessary data link bandwidth capacity if the raw data is transferred to a ground segment for image reconstruction.

Using lower rate A/D conversion in wide bandwidth SAR has the same effect as downsampling the original data. However, regular downsampling does not generate measurement matrices with RIP [53]. RIP can be achieved by randomly discarding some of the raw data [25] or any irregular transmission along the flight path [49]. But randomly discarding some of the regularly spaced samples cannot be easily implemented in practice by using lower rate A/D converters. Instead, jittered under-sampling which controls the maximum gap in the data is proposed [54]. First the A/D converter is programmed to sample data on a coarse but uniformly spaced grid. Then at the actual time of sampling, a sampling jitter is used to provide samples that lies almost randomly on a finer grid. Although jittered under-sampling requires accurate jitter control, it provides satisfactory results providing samples similar to desired random under-sampling. Also, a new A/D converter is proposed which performs sub-Nyquist sampling [55]. It presents a new hardware design for A/D converters to be used in CS applications which contain basically an RF front end and classical A/D converters.

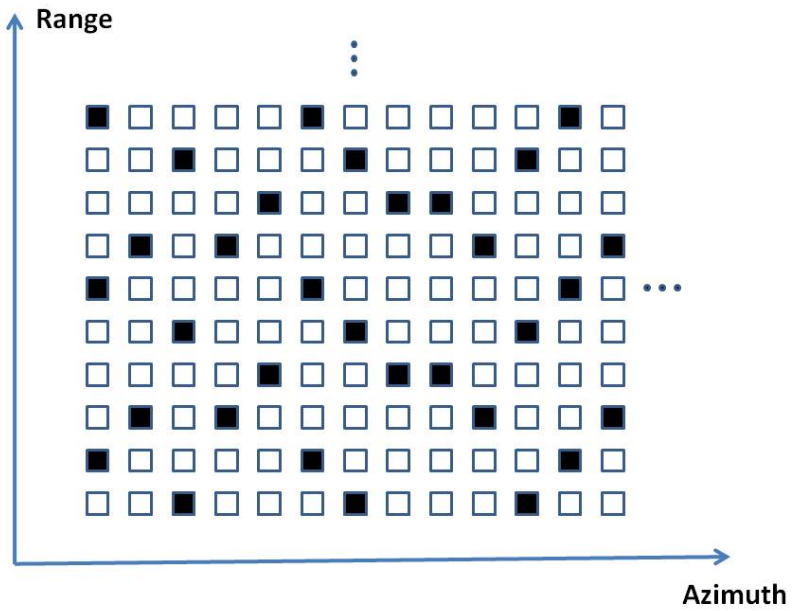

Figure 2.1: Example of the proposed under-sampling pattern for $K = 4$.

We propose a simple downsampling scheme that can be implemented using slower rate A/D converters, without any jitter control and hardware change. In this approach, the data is first downsampled by K in the range direction. The time of the initial sample at each azimuth location is pseudo-randomly chosen. This adds randomness to the data in the azimuth direction. Figure 2.1 presents an example of the under-sampling pattern for $K = 4$. The randomness in the range direction is obtained by randomly discarding a small ratio, L, of the downsampled data. This way, the prerequisites of CS are met despite the loss of a small portion of the data. As a result, this method of under-sampling reduces the rate of the A/D converter by a factor of K and reduces the memory requirement by a factor of $(1 - L)/K$. Table 2.1 lists the reduced A/D rate and the memory requirement for different values of parameters K and L. Note that the first row in the table is given as a reference and indicates the case of original data without any downsampling.

Table 2.1: A/D rate and the memory requirement for different values of parameters K and L.

K	**L**	**New A/D rate**	**Memory requirement**
1	0	1	100%
2	0.2	1/2	40%
3	0.1	1/3	30%
4	0.1	1/4	22.5%

2.3 The Proposed Autofocused Sparse SAR Image Reconstruction Technique in the Compressed Sensing Framework

The under-sampling scheme described in Section 2.2 results in the following measurement relation where the number of measurements is a fraction of the number of unknowns:

$$\mathbf{y_u} = \mathbf{\Phi}\ \mathbf{G_u}\ \mathbf{x} + \mathbf{w}, \tag{2.7}$$

where $\mathbf{y_u}$ and $\mathbf{G_u}$ represent the under-sampled measurement vector and the projection matrix respectively. Therefore, arbitrary scenes of reflectivity cannot be recovered from the available measurement data. However, if few objects with high reflectivity dominate the scene, sparse reconstruction techniques can provide reconstruction of these objects from the available data. Here, $\mathbf{\Phi}$ also corresponds to the under-sampled phase error matrix but it is not indicated as subscripted by u for the sake of brevity.

Assume the transformation matrix $\mathbf{\Psi}$ transforms the reflectivity vector $\mathbf{x}$ to a sparse domain,

$$\mathbf{y_u} = \mathbf{\Phi}\ \mathbf{G_u}\ \mathbf{\Psi}\ \alpha + \mathbf{w} = \mathbf{\Phi}\ \mathbf{A}\ \alpha + \mathbf{w}. \tag{2.8}$$

In the presence of phase errors, sparse SAR image reconstruction can be formulated as a constrained l_1 norm minimization problem:

$$\min_{\mathbf{\Phi},\alpha} \ \|\alpha\|_1 \qquad \textit{such that} \qquad \|\mathbf{y_u} - \mathbf{\Phi A}\alpha\|_2 \ \leq \ \sigma, \tag{2.9}$$

which is known as the Basis Pursuit Denoising (BPDN) formulation. While reconstructing sparse SAR images containing man-made targets, the number of pixels a target covers can be estimated by dividing the size of target area to the area of a pixel in the reconstructed SAR image. With this estimation and the transformation in which the image is sparse, one can set an upper limit τ to the l_1-norm of the target image. Then the SAR image reconstruction problem can be transformed into the following Lasso formulation [26, 56],

$$\min_{\mathbf{\Phi},\alpha} \ \|\mathbf{y_u} - \mathbf{\Phi A}\alpha\|_2 \qquad \textit{such that} \qquad \|\alpha\|_1 \ \leq \ \tau. \tag{2.10}$$

By integrating the phase error into the formulation, the required optimization should be carried out in terms of two sets of variables, α and $\mathbf{\Phi}$. To obtain an optimal solution, Eq. 2.10 can be solved by first finding optimal $\mathbf{\Phi}$ for a given α, then transforming the problem to a minimization over α alone [57]. To minimize the cost in Eq.2.10 for a given α, the phase error matrix $\mathbf{\Phi}$ that minimizes $\|\mathbf{y_u} - \mathbf{\Phi A}\alpha\|_2$ should be obtained. As detailed in Section 1.2 phase errors are assumed to be the same for all the data corresponding to an azimuth location, resulting in:

$$\min \ \|\mathbf{y_u} - \mathbf{\Phi A}\alpha\|_2^2 \ = \ \sum_{i=1}^{N} \min \ \|\mathbf{y_{ui}} - e^{j\phi_i}\mathbf{A_i}\alpha\|_2^2, \tag{2.11}$$

where $\mathbf{y_{ui}}$ is the partition of the measurement vector corresponding to the azimuth point i, $\mathbf{A_i}$ is the partition of the matrix $\mathbf{A}$ corresponding to the range bins of the azimuth point i, and N is the total number of azimuth points. Minimization of the term on the left side of the equation requires minimization of the individual terms in the summation, which can be expanded as:

$$\|\mathbf{y_{ui}} - e^{j\phi_i}\mathbf{A_i}\alpha\|_2^2 \ = \mathbf{y_{ui}}^H\mathbf{y_{ui}} - e^{j\phi_i}\mathbf{y_{ui}}^H\mathbf{A_i}\alpha - e^{-j\phi_i}\alpha^H\mathbf{A_i}^H\mathbf{y_{ui}} + \alpha^H\mathbf{A_i}^H\mathbf{A_i}\alpha. \tag{2.12}$$

For each term, the minimizing ϕ_i can be found as:

$$\frac{\partial}{\partial \phi_i} \|\mathbf{y_{ui}} - e^{j\phi_i}\mathbf{A_i}\alpha\|_2^2 \; = j\; e^{-j\phi_i}\alpha^H {\mathbf{A_i}}^H \mathbf{y_{ui}} - j\; e^{j\phi_i} {\mathbf{y_{ui}}}^H \mathbf{A_i}\alpha \; = \; 0. \tag{2.13}$$

The unique solution for ϕ_i can be obtained as:

$$\hat{\phi}_i \; = \; \angle\,(\alpha^H \; {\mathbf{A_i}}^H \; \mathbf{y_{ui}}). \tag{2.14}$$

With this result, Eq.2.10 can be reduced to an optimization over α only:

$$\min_{\alpha} \; \|\mathbf{y_u} - \mathbf{\Phi A}\alpha\|_2 \quad \textit{such that} \quad \|\alpha\|_1 \; \leq \; \tau, \quad \phi_i \; = \; \angle\,(\alpha^H \; {\mathbf{A_i}}^H \; \mathbf{y_{ui}}). \tag{2.15}$$

The same approach can also be applied for the BPDN formulation given in Eq. 2.9. Note that, since the min-min problem is not convex, the optimization in Eq. 2.15 has a non-convex feasible set. Therefore, local search techniques typically converge to a local minima of the problem. If the cost surface is such that the cost of the local minima is significantly higher than the global minima, a global optimization technique should be used. As illustrated in the next section, obtained results indicate that the cost of the local minima obtained by the proposed approach and the cost of the global minimum are acceptably close; therefore a slower converging global optimization technique such as Particle Swarm Optimization is not utilized for this problem.

At this stage of the formulation, to further improve the image reconstruction quality, TV penalty is integrated into the cost function [53, 58, 59, 60, 61]. Integrated TV penalty smooths the target and its environment and hence reduces the noise content of the image, which also increases the effectiveness of the phase error correction. By adding TV penalty, the cost function becomes:

$$\begin{aligned} &\min_{\mathbf{x}} \; \|\mathbf{y_u} - \mathbf{\Phi}\; \mathbf{G_u x}\|_2 + \beta\; TV(\mathbf{x}) \\ &\textit{such that} \qquad \|\mathbf{\Psi}^H \mathbf{x}\|_1 \; \leq \; \tau, \quad \phi_i \; = \; \angle\,(\mathbf{x}^H \;\; {\mathbf{G_{ui}}}^H \; \mathbf{y_{ui}}). \end{aligned} \tag{2.16}$$

Note that the relations $\alpha = \mathbf{\Psi}^H \mathbf{x}$ and $\mathbf{A}\alpha = \mathbf{G_u x}$ are used. Here, TV stands for total variation and defined as,

$$TV(\mathbf{x}) = \sum_{i,j} \sqrt{|\nabla_i x|_{i,j}^2 + |\nabla_j x|_{i,j}^2}\;, \tag{2.17}$$

where subscripts i, j denote pixel locations in a two dimensional image. ∇_i and ∇_j denote discrete gradients of the image in two directions and are given by,

$$(\nabla_i x)_{i,j} \;=\; x(i,j) \;-\; x(i-1,j), \tag{2.18}$$

$$(\nabla_j x)_{i,j} \;=\; x(i,j) \;-\; x(i,j-1). \tag{2.19}$$

The constrained optimization problem of Eq. 2.3 can be written as an unconstrained problem in the Lagrangian form:

$$\begin{aligned} \arg\min_{\mathbf{x}} \; g(\mathbf{x}) = \; \|\mathbf{\Psi}^H \mathbf{x}\|_1 + \beta \, TV(\mathbf{x}) \; + \gamma \, \|\mathbf{y_u} - \mathbf{\Phi} \; \mathbf{G_u x}\|_2^2 \\ \textit{such that} \; : \quad \phi_i \;=\; \angle \, (\mathbf{x}^H \;\; {\mathbf{G_{ui}}}^H \; \mathbf{y_{ui}}), \quad 1 \leq i \leq N. \end{aligned} \tag{2.20}$$

By using the non-linear conjugate gradient descent algorithm with backtracking line search [53, 62], a numerical solution to Eq. 2.20 can be obtained. There are more efficient algorithms published in the literature to solve l_1 minimization problems. The ones using Bregman methods are especially promising [63, 64, 65]. However, in all these techniques, the transformation in the data fidelity part of the cost function is a known matrix. But in our case, there is non-linear coupling between unknown reflectances and phase error. Therefore, the matrix contains the unknown $\mathbf{x}$, due to the multiplication by the phase error $\mathbf{\Phi}$, which leads us to use the conjugate gradient method. As part of the optimization iterations, the required gradient of the cost function can be computed as detailed in the Appendix A. Profiling Matlab [66] implementation of this numerical approach revealed that most of the CPU time is consumed by multiplications of large scale matrices. Therefore, by exploiting the structure of the involved matrices, significant computational improvements can also be achieved [67, 68].

2.4 Results of the Proposed Technique on Synthetic and Real SAR Data

In this section, results on both synthetic and real SAR data, obtained from MSTAR database [69], are presented. Raw SAR data is under-sampled as detailed in Section 2.2. Two different setups are used for the sparse reconstructions

of the synthetic and the MSTAR data. For the synthetic data, an A/D converter with 1/3 of the original rate is used and L is chosen as 0.1, which results in 70% memory reduction. For the MSTAR data, half rate A/D converter is used and L is chosen as 0.2, which results in 60% memory reduction. Hence, synthetic data results are obtained by using only 30% of the original raw data while the MSTAR results are obtained by using only 40% of the original raw data.

The parameters β and γ in Eq. 2.20 can be used to adjust the relative weights of the different components in the cost function. For example, increasing the weight of the TV part smooths the noisy areas containing sudden changes in the image. Because this work is not aimed to put forward specific properties in the images, equal weights ($\beta = \gamma = 1$) are chosen for balanced contribution of different parts in the cost function unless otherwise specified.

2.4.1 Synthetic Data Reconstructions

The synthetic image used in the trials is shown in Figure 2.2.(a). Reconstructed images of the artificial scene by Polar Format Algorithm (PFA) [6] for the same phase error, but at two different noise levels are shown in Figures 2.2.(b) and 2.2.(c) respectively. Both of these reconstructions are obtained using 3 times more data than the proposed sparse reconstruction technique.

In synthetic data experiments, the transformation $\mathbf{\Psi}$, which maps $\mathbf{x}$ to the sparsity domain, is chosen as the identity matrix. This works quite well when the speckle noise is negligible. However, the reconstruction performance degrades when the speckle noise increases since noise starts having large projection on the impulsive basis components.

The obtained sparse reconstructions are shown in Figures 2.2.(d) and 2.2.(e). In the case with higher SNR (Figure 2.2.d), CS-PE-TV works quite well, almost completely removing the phase error. In the case with lower SNR (Figure 2.2.e), CS-PE-TV concentrates much of the energy of the target and corrects phase error effects very well. However, it does not wholly reconstruct the original target and

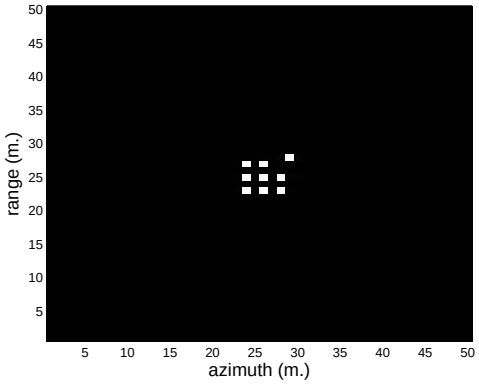

(a)

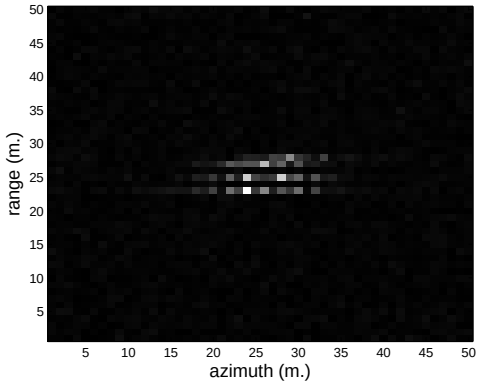

(b)

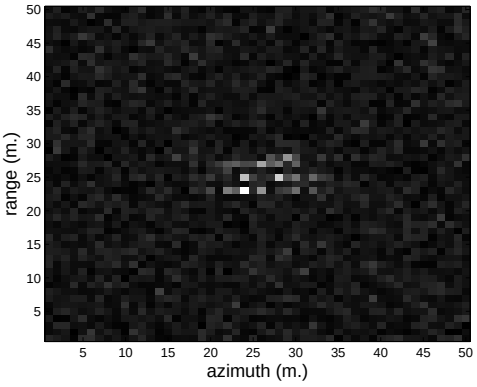

(c)

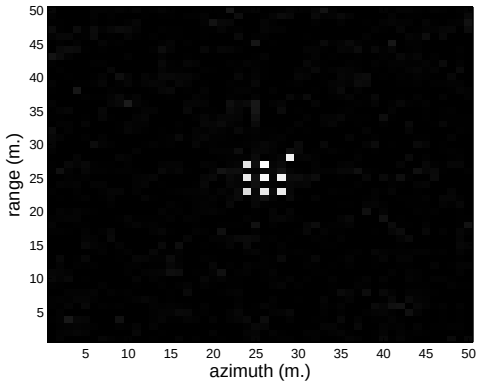

(d)

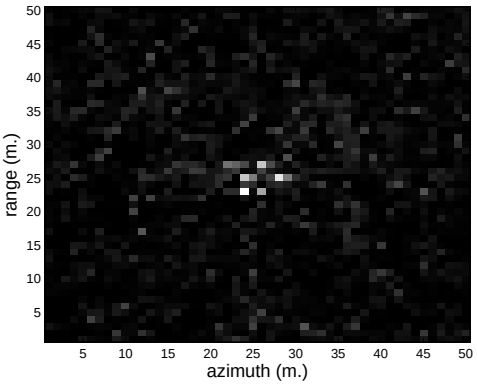

(e)

Figure 2.2: The synthetic images by PFA and the reconstructions by CS-PE-TV are illustrated. (a) Original reflectivity image. (b) Image with phase error and speckle noise (SNR = 31 dB) reconstructed by PFA. (c) Image with phase error and speckle noise (SNR = 19 dB) reconstructed by PFA. (d) Image with phase error and speckle noise (SNR = 31 dB) reconstructed by CS-PE-TV. (e) Image with phase error and speckle noise (SNR = 19 dB) reconstructed by CS-PE-TV.

has some artifacts left in the scene. Compared to the case with higher SNR, the main reason for the performance degradation in the case with lower SNR is the speckle noise, which starts having larger projections on the sparse basis components.

2.4.2 MSTAR Reconstructions

MSTAR database [69] contains publicly available SAR data of several target types. The ones used in the reconstruction trials are illustrated in the row (a) of Figure 2.3. Each contains a target in an environment with high speckle noise.

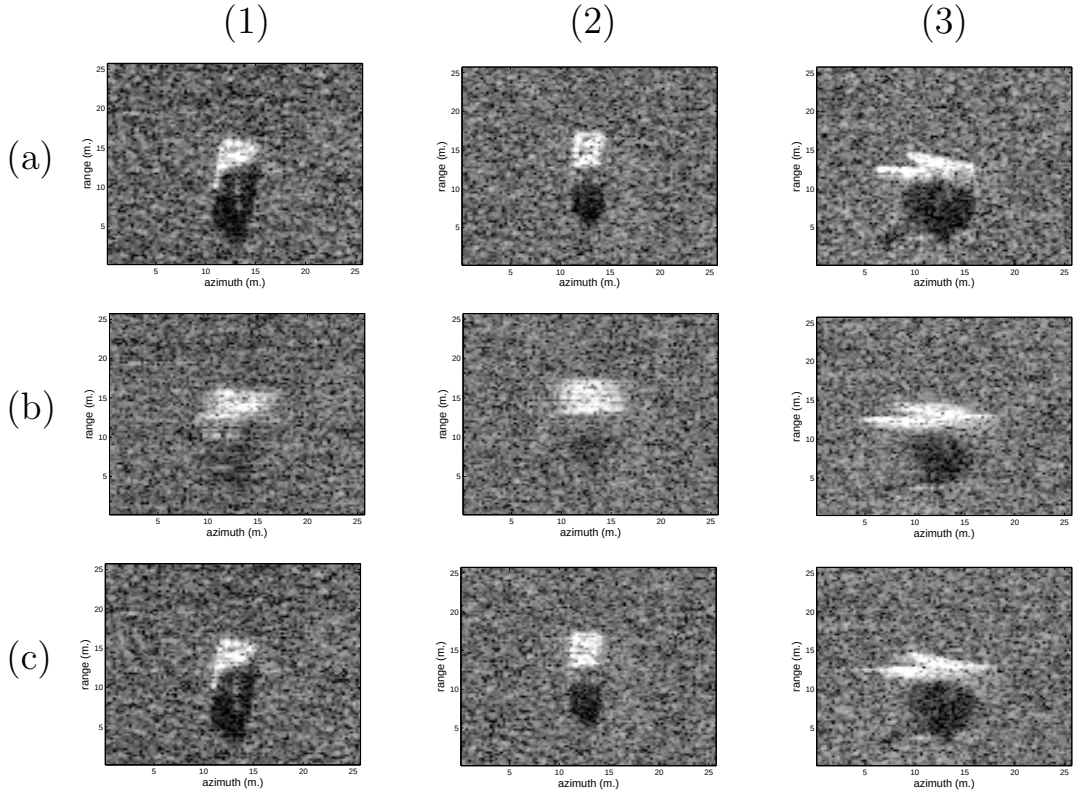

Figure 2.3: Three target images of MSTAR database that are used in the trials. All the images are reconstructed by PFA. Row (a) gives the original images. Row (b) presents the images with inserted phase error. Row (c) shows the reconstructions of images autofocused by PGA.

These images are reconstructed using PFA. The row (b) of Figure 2.3 gives the same images with artificially inserted phase error. They are reconstructed again

by PFA. The applied phase error characteristics have been given in Figure 2.5. In order to corrupt the phase of the MSTAR images, corresponding raw data is needed. But MSTAR database contains only the complex valued SAR images. Therefore, the procedure explained in [70] is applied to convert SAR images to raw SAR data. Then phase error is inserted to raw SAR data as an exponential multiplication [11].

Row (c) of Figure 2.3 shows the images reconstructed by PFA and autofocused by the Phase Gradient Algorithm (PGA) [17, 18]. PGA first center shifts the brightest pixels in each range bin, then applies windowing to suppress the effects of other possible targets in the same range bin. Finally, it estimates the phase error in the azimuth dimension and applies phase correction. Generally, one to three iterations of the PGA are sufficient to estimate and correct the phase errors successfully.

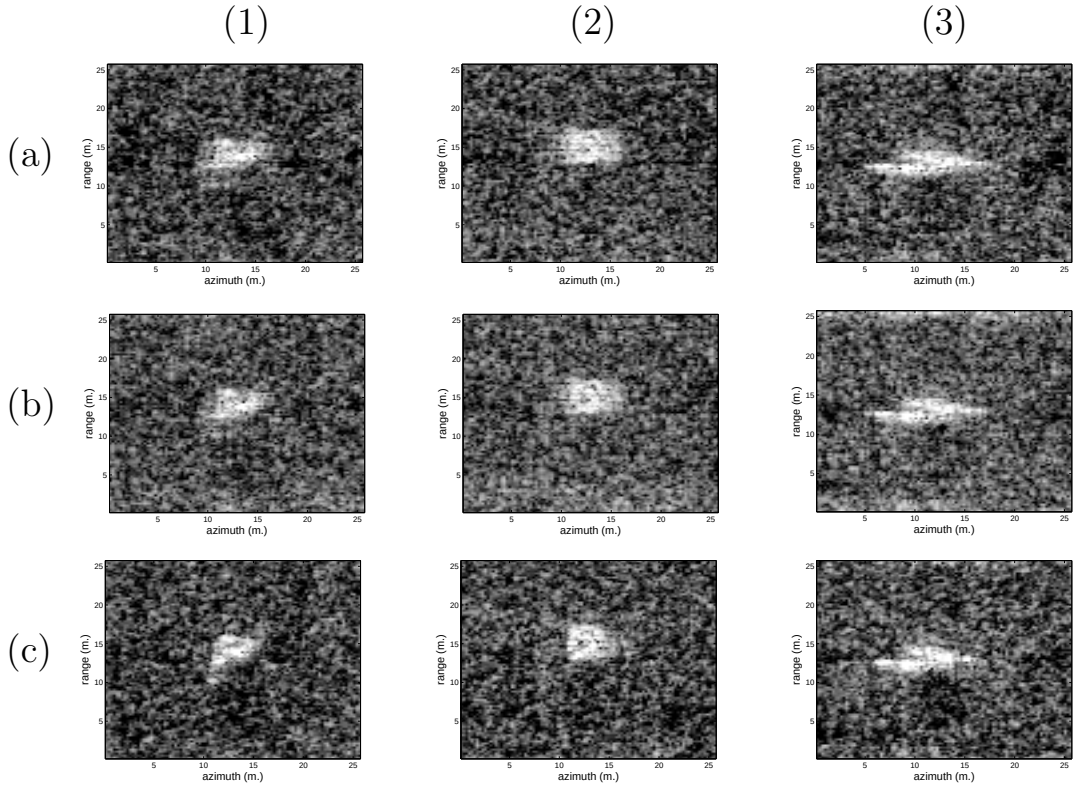

Figure 2.4: Three target images of MSTAR database that are used in the trials. Row (a) gives the results of CS reconstructions. Row (b) presents the results of CS-PE reconstructions. Row (c) gives the images reconstructed by CS-PE-TV.

The results obtained by the proposed sparse SAR image reconstruction technique on the MSTAR data are illustrated in Figure 2.4. For CS reconstructions, only a fraction of the whole data, obtained by the method explained in Section 2.2, is used. Since wavelet frames are appropriate for representing SAR images containing man-made targets, Daubechies-4 wavelets are used as the sparsity transform in the trials with MSTAR data.

For comparison purposes, row (a) of Figure 2.4 shows the results of sparse reconstruction with no phase error correction, which will be referred to as CS reconstructions. Row (b) displays the results for the case of applying autofocused sparse reconstruction without a TV penalty, which will be referred to as CS-PE reconstructions. This reconstruction is obtained by solving Eq. 2.20 with $\beta = 0$. The results of the proposed CS-PE-TV reconstructions are presented on row (c) of Figure 2.4.

As expected, CS reconstructions suffer from significant degradation due to uncompensated phase error. The images reconstructed by CS-PE show improved phase error correction compared to CS results. But the noisy nature of the images prevents further improvements. Adding TV penalty into the cost function improves the overall image reconstruction quality and success of phase error correction. This deduction is clearly demonstrated by comparing the results of CS-PE-TV to the results of CS-PE. The CS-PE-TV reconstructs the images and autofocuses them simultaneously with success.

The phase error applied to the images and its estimate obtained by the application of CS-PE-TV are shown in Figure 2.5. The estimated phase error closely follows the general form of the applied phase error. The root mean square error of the estimation is only 1.9% of the radar's wavelength.

In order to quantify and compare the image reconstruction performance of the proposed CS-PE-TV technique especially on the MSTAR data, the following metrics are used:

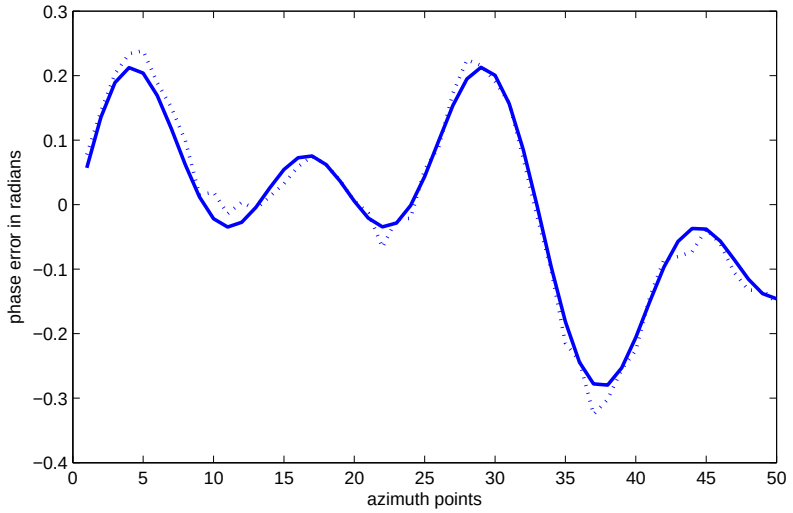

Figure 2.5: The phase error applied to the image (solid line) and the phase error estimate (dotted line). Y-axis units represent the fractions of the SAR wavelength.

1. Mean Square Error, which is defined as [71]:

$$MSE = \frac{1}{N^2} \parallel |\mathbf{x}| \; - \; |\hat{\mathbf{x}}| \parallel_2^2, \tag{2.21}$$

where $\mathbf{x}$ is the original image, $\hat{\mathbf{x}}$ is the reconstructed image, and N^2 is the total number of pixels in the image.

2. Target-to-Background Ratio (TBR) [71, 72] : This is the ratio of the absolute maximum of the target region to the absolute average of the background region. It gives an indication of how target pixels are discernible with respect to background pixels:

$$TBR = 20 \; log_{10} \left(\frac{max_{i \in T} \left(|(\mathbf{x})_i| \right)}{\frac{1}{N_B} \; \sum_{j \in B} \; |(\mathbf{x})_j|} \right), \tag{2.22}$$

where $\mathbf{x}$ is the image and N_B is the number of pixels in the background region of the image. T and B represent target and background regions, respectively.

3. Entropy of the image [71]: This is a metric related to sharpness of the

image:

$$H(\mathbf{x}) = -\sum_i p_i \log_2 p_i, \tag{2.23}$$

where the discrete variable p contains the histogram counts of the image $\mathbf{x}$. Entropy is small for sharper images so it is preferable for an algorithm to result in low entropies for image formation.

These metrics give indications about the performance of the reconstructions especially on the target classification applications. The quantitative performance metrics for the images illustrated in Figure 2.4 are given in Table 2.2. The table

Table 2.2: Performance metrics for the imagery reconstructed by different methods.

		MSE	**TBR**	**Entropy**
Target (1)	**PFA**	$6.2.10^{-3}$	27.02	2.88
	PFA-PGA	$\mathbf{2.5.10^{-4}}$	29.55	2.50
	CS	$5.7.10^{-3}$	30.68	2.50
	CS-PE	$5.2.10^{-3}$	28.91	2.76
	CS-PE-TV	$3.6.10^{-3}$	**31.59**	**2.42**
Target (2)	**PFA**	$7.7.10^{-3}$	23.99	3.34
	PFA-PGA	$\mathbf{1.9.10^{-3}}$	27.08	2.95
	CS	$6.8.10^{-3}$	27.56	3.01
	CS-PE	$6.0.10^{-3}$	25.65	3.29
	CS-PE-TV	$4.5.10^{-3}$	**28.41**	**2.94**
Target (3)	**PFA**	$10.9.10^{-3}$	24.31	2.96
	PFA-PGA	$\mathbf{9.3.10^{-4}}$	26.23	2.80
	CS	$10.4.10^{-3}$	27.48	2.73
	CS-PE	$9.8.10^{-3}$	24.77	3.13
	CS-PE-TV	$7.2.10^{-3}$	**30.23**	**2.42**

lists the results for three targets which are reconstructed by using five different

techniques. For each target the first row lists the metrics of the images reconstructed by PFA. The second row lists the results for the images reconstructed by PFA and autofocused by PGA. The results of the CS, CS-PE and CS-PE-TV techniques are listed in the third, fourth and fifth rows respectively. Note that these results can be improved by post processing the images. However, we are interested in comparing the performances of the applied methods alone, so no post processing is performed on the images.

PFA-PGA, which makes use of data obtained at Nyquist sampling rate, gives the best results in terms of the MSE metric. For the TBR and entropy metrics the CS-PE-TV technique provides better results than the PFA-PGA technique. The main disadvantage of the CS-PE-TV method compared to the PFA-PGA method is the computational complexity which currently limits the application of the CS-PE-TV technique to offline reconstructions. However, with the rapid advances in signal processor hardware, the application of CS to SAR image reconstruction can become feasible in the near future.

PFA performs poorly by all metrics. Even the CS technique performs better than the PFA. This result confirms the statement that p-norm regularizations reduce the amplitude and phase irregularities for $p < 2$ [28]. The CS-PE is an improvement over CS for the MSE metric. Phase error model integration to the problem tries to compensate the effects of the phase error and guarantees more localized target images. But TBR and the entropy of the image degrade with CS-PE as compared to CS. Because the lack of TV penalty in the CS-PE technique increases the entropy. TV penalty, in the CS technique smooths the constant areas and thereby reduces the average of the background region in the TBR formulation.

With phase error model integrated and the TV penalty added, CS-PE-TV outperforms all the other techniques (except the PFA-PGA technique in MSE parameter as indicated above). Almost all the metrics listed in the table indicate an improvement for the images reconstructed by the CS-PE-TV technique. Therefore, adding phase error in the signal model embeds autofocus property into the image reconstruction. Furthermore, adding in TV penalty to the cost

function improves the overall reconstruction performance for SAR images with high speckle noise. In conclusion, these results demonstrate that the proposed CS-PE-TV technique provides robust, simultaneous SAR image reconstruction and autofocus.

The main drawback of the CS-PE-TV technique is its high computational complexity as indicated before. Non-Linear Conjugate Gradient Descent algorithm demands high computational power to apply it to SAR image reconstruction. Retaining the advantages of CS methodology on SAR image reconstruction, a new technique applying EMMP algorithm is proposed in the next chapter to improve the image reconstruction speed. EMMP algorithm is greedy and computationally less complex, which results fast reconstructions compared to Non-Linear Conjugate Gradient Descent algorithm based techniques. The next chapter gives details of the proposed sparse SAR image reconstruction technique based on EMMP algorithm [73, 74, 75].

Chapter 3

Autofocused Sparse SAR Image Reconstruction by EMMP Algorithm

As detailed in Chapter 2, CS based radar has several advantages such as reduced memory size or decreased A/D converter rates or possibility of eliminating the match filtering process [23]. SAR image reconstruction by using sparsity driven penalty function has been investigated in [23, 24, 9, 71, 10]. SAR image reconstruction by CS is generally formulated as a convex l_1 norm minimization problem and it is solved by either linear programming or greedy pursuit algorithms. Although these techniques do not consider phase errors in SAR image reconstruction problem, the proposed techniques in [76], [29] and [77] provide sparse reconstructions in the presence of phase errors. However, compared to the commonly used SAR autofocus techniques, these approaches require significantly longer computational times.

In the proposed autofocused SAR image reconstruction technique introduced in Chapter 2, non-Linear conjugate gradient descent algorithm is used to find the optimized solution for a sparsity driven cost function. Non-linear conjugate gradient descent algorithm has a high computational complexity requiring significant

time and resources. To overcome these shortcomings, a novel autofocused SAR reconstruction technique is proposed in this chapter. This technique is based on a new sparse reconstruction method called Expectation Maximization Matching Pursuit (EMMP) algorithm [73]. The EMMP algorithm uses the compressive measurements as incomplete data and iteratively applies expectation and maximization (EM) steps to reliably estimate the complete data which corresponds to dominant reflectors in the scene of interest. The objective of EM iterations is to provide more reliable estimates to the complete data so that accurate and efficient estimation of the fewer number of parameters in each disjoint parameter set can be conducted in the maximization step. Once, more accurate estimates for the parameters are available, marginal contribution of a disjoint set can be estimated by subtracting the expected marginal contributions of the other remaining set of parameters from the available measurements, which is called as the expectation step. In EMMP algorithm, also the phase error can be estimated at each step of the iterations together with the reflectivity distribution. The algorithm is greedy, therefore it is not assured to obtain the global optima. However, its computational efficiency makes it a viable choice in practical applications. As will be detailed in this section, the EMMP based autofocused SAR reconstruction technique has smaller reconstruction errors compared to l_1 norm minimization[78]. Hence, both the accuracy and convergence rate of the iterations significantly increase, enabling fast and high resolution SAR image reconstructions even under severe phase errors. Note that, in addition to the preliminary results presented in [74], the proposed approach is extended to perform autofocus as part of the EMMP iterations [75].

3.1 Simultaneous Reconstruction and Autofocus of Sparse SAR Images Based on EMMP Algorithm

It is common in real life applications to have signals that have sparse representations in known dictionaries, such as Fourier, wavelet or a union of them.

Sparse signals can be represented closely as a linear combination of a few of the dictionary elements.

One important application of SAR systems is imaging of man-made structures. Since, typically reflection from man-made structures are significantly stronger than that of the piece of a terrain in a resolution cell, reflectivity distribution over the imaged area can be modeled as a sparse distribution over an appropriate set of vectors such as wavelets.

CS techniques guarantee reliable reconstruction of a sparse signal of length N if the measurement matrix satisfies Restricted Isometry Property (RIP) and the number of measurements are at least $O(K \log(N/K))$ where K is the level of sparsity of the signal [52], which can be significantly smaller than N. Thus, for sparse reconstructions, the required number of samples can be significantly reduced below the Nyquist rate, resulting in important hardware savings. To exploit the potential reduction in the sampling rate, the method described in [76] can be used to under-sample the measured data. Assuming that the reflectivity vector is sparse in the column space of a given matrix $\mathbf{\Psi}$ with representation coefficients α, measurements model given in Eq.2.8 can be written equivalently as:

$$\mathbf{y_u} = \mathbf{\Phi}\ \mathbf{G_u}\ \mathbf{\Psi}\ \alpha + \mathbf{w} = \mathbf{\Phi}\ \mathbf{A}\ \alpha + \mathbf{w}. \tag{3.1}$$

Here matrix $\mathbf{A}$ is known but matrix $\mathbf{\Phi}$, which captures the phase errors is an unknown matrix. In the absence of phase errors, the SAR image reconstruction has been formulated in CS methodology in two different approaches previously. In Basis Pursuit Denoising (BPDN) [26] formulation, the scene with minimum l_1 norm is reconstructed such that the resulting fit error to measurements is less than a threshold σ. In LASSO formulation [56], the scene with a known l_1 norm τ, is chosen to minimize the fit error. Although in principle these formulations are equivalent for a properly chosen (σ, τ) pair, it is not straightforward to determine σ for SAR image reconstructions especially if the terrain reflectivity is highly variable. However, an appropriate choice for τ can be obtained based on the size and reflectivity of the dominant reflectors in the imaged area. Hence, it is easier to choose a proper τ, to the l_1-norm of the target. Therefore, LASSO formulation

is more suitable for SAR image reconstructions with dominant reflectors in the target scene.

In CS applications, it is desired to obtain the most sparse signal representation, which requires to use l_0 norm minimization [32, 33]. Since l_0 norm optimization requires combinatoric search that is not feasible for SAR applications, generally it is relaxed to l_1 norm minimization problem as in the above formulations. It is proven that l_0 and l_1 norm minimization problems provide the same solution if α is sparse and A holds the RIP [43, 44]. Unfortunately, it is difficult to prove that a matrix holds the RIP. However, a few classes of matrices have desired RIP [33, 43, 44] which include random matrices with independent identically distributed entries, Fourier ensemble matrices, and general orthogonal measurement ensembles.

Unlike BPDN and LASSO formulations, the proposed EMMP approach provides a near optimal solution to the following l_0 norm problem:

$$\min_{\alpha} \ \|\mathbf{y_u} - \mathbf{A}\alpha\|_2 \quad \textit{such that} \quad \|\alpha\|_0 \ \leq \ K, \tag{3.2}$$

where K is the sparsity level of the signal. Sparsity level K can be estimated for man-made targets based on the area of these targets in the scene. Hence, it is actually easier to choose K, because the choice for τ in the LASSO formulation also requires reflectivity information about these targets. To obtain a sparse and autofocused reconstruction, the optimization should be carried out in terms of two sets of variables, α and $\mathbf{\Phi}$ to account for the phase error:

$$\min_{\alpha,\mathbf{\Phi}} \ \| \ \mathbf{y_u} \ - \ \mathbf{\Phi A}\alpha \ \|_2 \quad \textit{such that} \quad \|\alpha\|_0 \ \leq \ K. \tag{3.3}$$

By using the Expectation Maximization (EM) [79] framework, the EMMP algorithm operates between two spaces: the incomplete and complete data spaces. The incomplete data space corresponds to the available SAR measurements $\mathbf{y_u}$, and the complete data space is the set of measurement vectors $\mathbf{y_i}$ that would correspond to the contribution of a single scatterer in the scene. The mapping

between the complete and incomplete data spaces is:

$$\begin{aligned} \mathbf{y_u} &= \mathbf{\Phi}\ [\mathbf{A_1 A_2} \dots \mathbf{A_N}]\ [\alpha_1 \alpha_2 \dots \alpha_N]^T\ +\ \mathbf{w} \\ &= \mathbf{\Phi}\ \sum_{i=1}^{N} \alpha_i \mathbf{A_i}\ +\ \mathbf{w}\ . \end{aligned} \tag{3.4}$$

Assuming that only K of α_i's are nonzero, *i.e.*, α_i is K-sparse, the measurements can be written as:

$$\mathbf{y_u} = \mathbf{\Phi}\ \sum_{i=1}^{K} \mathbf{y_i}\ +\ \mathbf{w}\ , \tag{3.5}$$

where $\mathbf{y_i} = \alpha_i \mathbf{A_i}$, which is what should have been measured if there were only the i^{th} reflector in the scene and there were no noise and phase error.

In the presence of phase errors, to minimize the cost in Eq.3.3, the problem can be solved in two sequential steps by first finding optimal $\mathbf{\Phi}$ for a given α, then solving the optimization over α alone [57]:

$$\min_{\alpha}\ f_0(\alpha) \qquad \textit{such that} \qquad \|\alpha\|_0\ \leq\ K, \tag{3.6}$$

where,

$$f_0(\alpha)\ =\ \inf_{\mathbf{\Phi}}\ \{\ \|\ \mathbf{y_u}\ -\ \mathbf{\Phi A}\alpha\ \|_2\ \}\,. \tag{3.7}$$

To minimize the cost in Eq.3.7 for a given α, the phase error matrix $\mathbf{\Phi}$ that minimizes $\|\mathbf{y_u} - \mathbf{\Phi A}\alpha\|_2$ should be obtained. Phase errors generally do not depend on the range axis so they are assumed to be the same for all the data corresponding to a certain azimuth location [11]. Then the minimization can be formulated equivalently as:

$$\min\ \|\mathbf{y_u} -\ \mathbf{\Phi A}\alpha\|_2\ =\ \sum_{\theta}\ \min\ \|\mathbf{y}_\theta - e^{j\phi_\theta}\mathbf{A}_\theta\alpha\|_2, \tag{3.8}$$

where $\mathbf{y}_\theta$ is the partition of the under-sampled measurement vector, $\mathbf{A}_\theta$ is the partition of the matrix $\mathbf{A}$ and $e^{j\phi_\theta}$ is the phase error, all for corresponding to the look angle θ. Minimization of the term on the left side of the equation requires minimization of the individual terms in the summation. In this formulation, the unique solution for phase error estimate ϕ_θ, for each look angle θ can be obtained as:

$$\hat{\phi}_\theta\ =\ \angle\ (\alpha^H\ \mathbf{A}_\theta{}^H\ \mathbf{y}_\theta). \tag{3.9}$$

With this result, Eq.3.3 can be reduced to an optimization over α only:

$$\min_{\alpha} \|\mathbf{y_u} - \mathbf{\Phi A}\alpha\|_2 \qquad \textit{such that} \qquad \|\alpha\|_0 \leq K, \\ \phi_\theta = \angle\,(\alpha^H\, {\mathbf{A}_\theta}^H\, \mathbf{y}_\theta). \tag{3.10}$$

These sequential steps are combined within the EMMP algorithm, which is summarized in Figure 3.1. In the algorithm, **CD** corresponds to the complete data matrix, **r** corresponds to the residual vector and ϵ corresponds to the termination criteria which can be set to the average energy of background pixels around the region of interest. The inputs of the EMMP algorithm are the measurement matrix $\mathbf{A}$, the measurements $\mathbf{y_u}$, the sparsity level K, and a termination parameter ϵ. Initially, the complete data matrix is set to zero and the residual vector is initialized to $\mathbf{y_u}$. As in the EM algorithm, in EMMP algorithm iterations, given estimates for $\mathbf{y_i}$ and $\mathbf{\Phi}$, the i^{th} sparse component of α is found as the best matching vector among the columns of $\mathbf{A}$ to $\mathbf{\Phi}^{-1}\mathbf{y}_i$, for $1 \leq i \leq K$. The selected index list and the complete data matrix are updated. Then, $\mathbf{\Phi}$ is re-estimated by using the obtained α, and the iterations are restarted. The iterations are continued until the termination criteria or a pre-determined number of iterations are reached. Determining the correct K value is an important issue related to the performance of the proposed algorithm and this issue is investigated in Section 3.3

3.2 Simulation Results

We tested the proposed technique to illustrate its performance on synthetic data as well as data from MSTAR database [69]. For synthetic data, an A/D converter operating at one-third of the Nyquist rate is used. For Slicy data of MSTAR database, an A/D converter operating at one-fourth of the Nyquist rate is used. For military target data of MSTAR database, a half rate A/D converter is used. In addition to the rate reduction of the A/D converter, another 10% reduction on the obtained samples is achieved by using pseudo-random sampling scheme detailed in [76].

MATLAB implementation of the proposed EMMP algorithm running on a

Input:

A measurement matrix

y_u measurement vector

K sparsity level

ϵ termination criteria threshold

Initialization:

$\Phi = I$ phase error estimate

$CD = 0$ complete data matrix

$r = y_u$ residual vector

while loop repeat until $\frac{1}{N}\|\mathbf{r}\|_2^2 < \epsilon$

for $i = 1 : K$

Expectation:

$\hat{\mathbf{y}}_i = \mathbf{y_u} - \sum_{j \neq i} \mathbf{CD}(:, j)$

Maximization:

$proj = \mathbf{A}^T \hat{\mathbf{y}}_i$

$\lambda = arg\ max|proj|$

$\mathbf{p} = \mathbf{A}(:, \lambda)$

$\mathbf{y_i} = \mathbf{p}\ \mathbf{p}^T \hat{\mathbf{y}}_i$

Keep and Update:

$\lambda_L(i) = \lambda$ λ list

$\mathbf{CD}(:, i) = \mathbf{y_i}$

end for loop

calculate residual $\mathbf{r} = \mathbf{y_u} - \sum_{j=1}^{K} \mathbf{CD}(:, i)$

$\hat{\mathbf{A}} = \mathbf{A}(:, \lambda_L)$

$\alpha = zeros(N, 1)$

$\alpha(\lambda_L) = \min\|\mathbf{y_u} - \sum_{j=1}^{K} \alpha(\lambda_L(j))\hat{\mathbf{A}}(:, j)\|_2$

Phase Error Estimate:

$\hat{\phi}_\theta = \angle\ (\alpha^H\ \mathbf{A}_\theta^H\ \mathbf{y}_\theta)$

$\mathbf{y_u} = \mathbf{\Phi}^{-1}\mathbf{y_u}$

end while loop

Output: $\mathbf{x} = \mathbf{\Psi}\alpha$ solution vector

Figure 3.1: EMMP algorithm with phase error estimation.

laptop converges in about 20 iterations in about 20 seconds to 5 minutes depending on the size of the image, which is significantly faster than alternative gradient descent based optimization techniques for CS reconstructions. For real-time applications, the proposed approach can be implemented on off-the-shelf processor boards to further reduce the computation time.

3.2.1 Synthetic Data Results

The proposed technique is first applied on the synthetic SAR data. To provide a benchmark, the synthetic SAR data with no phase error is processed with Polar Format Algorithm (PFA) and the resultant image shown in Figure 3.2.(a) is obtained. To investigate effect of motion errors, the synthetic SAR data is distorted by phase errors at each azimuth vantage point. The result obtained by the PFA algorithm is shown in Figure 3.2.(b). For comparison, reconstructed SAR image by using the well known Phase Gradient Autofocus algorithm (PGA) [18] is shown in Figure 3.2.(c). Usually, three iterations of PGA is sufficient to compensate phase errors reasonably. As seen from Figure 3.2.(c), although the image is corrected to some extent compared to Figure 3.2.(b), phase error related degradations are still visible. In Figure 3.2.(d), the reconstruction obtained by using the proposed EMMP based approach is shown. Although this reconstruction is obtained by using only 30% of the data required by the PGA technique, it is visibly better focused than the result of PGA shown in Figure 3.2.(c)

3.2.2 Slicy Data Results

The results obtained for two types of Slicy target are shown in Figure 3.3. The first row presents PFA reconstructions with no phase error. The PFA reconstructions with synthetically induced phase error are shown in the second row. Reconstructions by PFA and autofocused by PGA technique are given in the third row. The fourth row presents the reconstructions obtained by the proposed EMMP technique. Note that the proposed algorithm uses only 22.5% of the raw data.

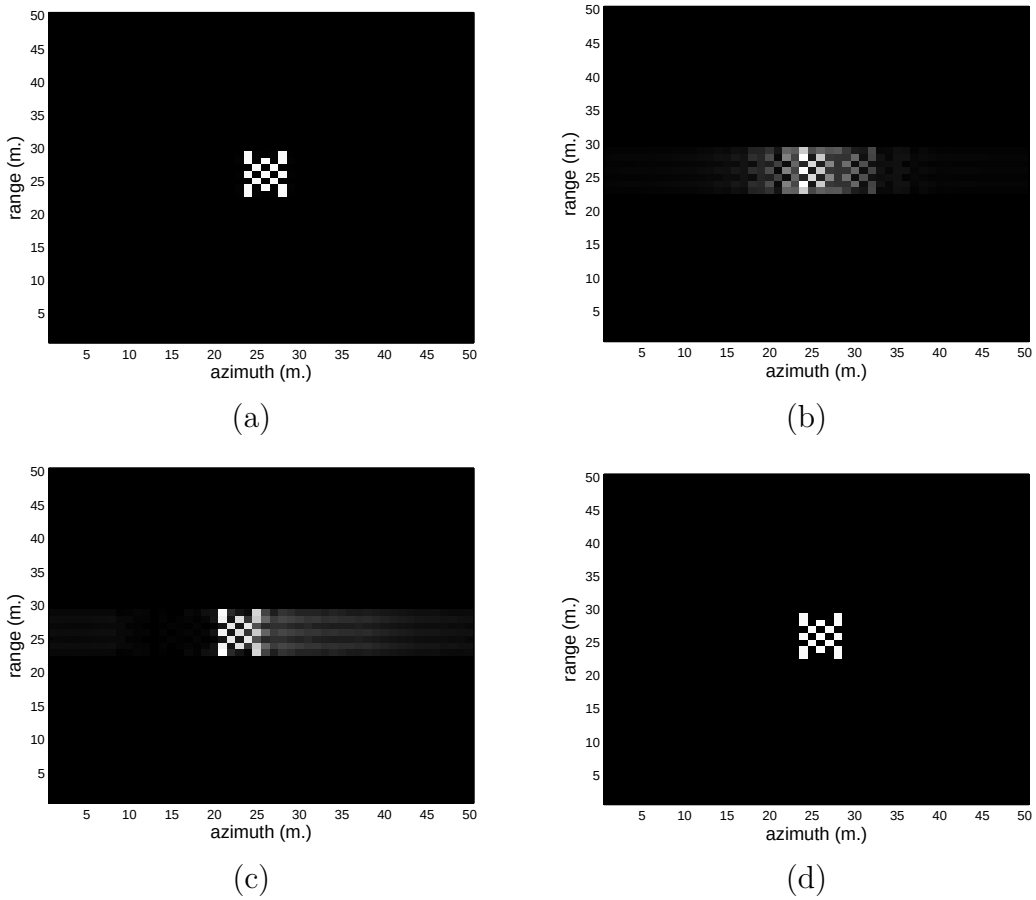

Figure 3.2: The synthetic target reconstructions are illustrated. (a) The original image reconstructed by PFA. (b) The original image with inserted phase error. (c) The autofocused image by PGA. (d) Image reconstructed by the proposed technique. While the images (a), (b) and (c) use data obtained at the Nyquist rate, for (d) the EMMP uses only 30% of the Nyquist rate data.

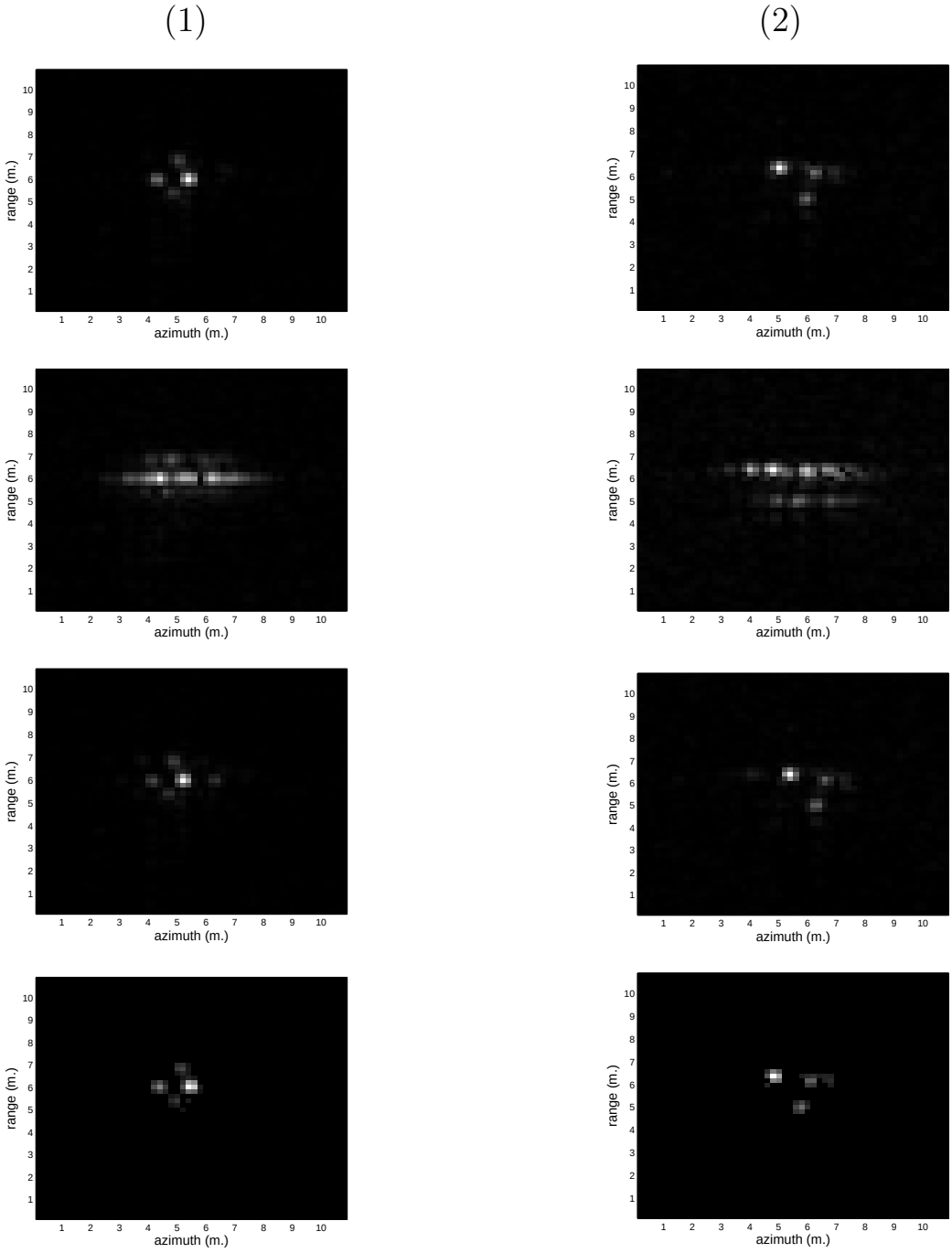

Figure 3.3: Two Slicy target reconstructions are shown in two columns. First row: PFA reconstructions with no phase errors; Second row: PFA reconstructions with synthetically induced phase errors; Third row: PFA-PGA reconstructions; Fourth row: proposed EMMP reconstructions. While PFA and PFA-PGA use data obtained at the Nyquist rate, in Slicy target reconstructions the EMMP uses only 22.5% of the Nyquist rate data.

The results show that the quality of the reconstructions of the proposed EMMP technique are better than that of the PFA-PGA technique while the proposed EMMP technique requires a fraction of the data for reconstruction. Even though some minor blurs caused by phase errors left in PFA-PGA reconstructions, phase error degradations are almost totally removed from the images reconstructed by the proposed EMMP technique. Unlike the previously proposed CS SAR reconstruction techniques, the processing time of the proposed EMMP technique is also comparable to the PFA-PGA technique.

To illustrate the extend of autofocusing provided by the proposed algorithm, significantly large phase error is synthetically induced in the raw data. As shown in Figure 3.4, the proposed EMMP technique provides an acceptable estimate to the synthetically induced phase error.

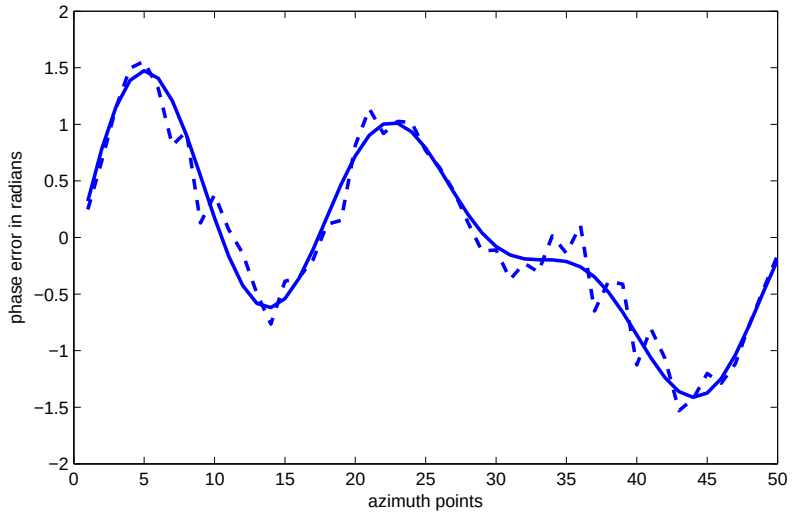

Figure 3.4: The synthetic (solid line) and the estimated phase error (dashed line) in radians.

To provide more objective comparisons between the the proposed EMMP and the PFA-PGA techniques, the metrics MSE, TBR and Entropy defined in Section 2.4.2 are used. Table 3.1 lists these metrics for the images illustrated in Figure 3.3. The data presented in Table 3.1 indicates that PFA-PGA technique has a better performance only for the MSE metric of the Slicy 1 target. For all other cases, the EMMP technique outperforms the PFA-PGA technique. Note that,

Table 3.1: Metrics for the Slicy target imagery reconstructed by PFA-PGA and the proposed EMMP techniques. The PFA-PGA technique, which is reconstructed by PFA and autofocused by PGA uses whole raw SAR data. The proposed EMMP technique uses only 22.5% of the Nyquist rate data.

	Slicy Target 1			**Slicy Target 2**		
	MSE	**TBR**	**H**	**MSE**	**TBR**	**H**
PFA-PGA	$4.0.10^{-3}$	41.1	4.91	$9.3.10^{-4}$	36.0	4.59
EMMP	$9.1.10^{-3}$	∞	0.14	$5.8.10^{-5}$	∞	0.12

elimination of the speckle by the EMMP technique causes the TBR metric to become infinity. The results show that the EMMP technique serves well for the target classification without further windowing and speckle noise removal. It is important to note that, unlike the classical PFA-PGA technique, the proposed EMMP technique has variable ϵ and K parameters that can be adjusted for the target class of interest to provide significant control over the reconstructions.

3.3 Effect of Sparsity Parameter on Image Reconstruction Quality of the Proposed Technique Based on EMMP Algorithm

In this section the effect of correct determination of the sparsity parameter, K, on the reconstructed image quality is investigated. Military target image of MSTAR database is used, with 40% of the Nyquist rate data, in reconstructions by the proposed technique. Figure 3.5.(a) gives the original image used in this trials. The image has high speckle noise content to indicate the incorrect determination of K parameter increases the noise level of the reconstructed image. Figs. 3.5.(b)-(f) illustrate the resultant images reconstructed by the proposed EMMP technique for a range of sparsity level K.

Figure 3.5 illustrates that for K, lower than the actual sparsity level of the target, reconstructed images lack important features of the target. For K values

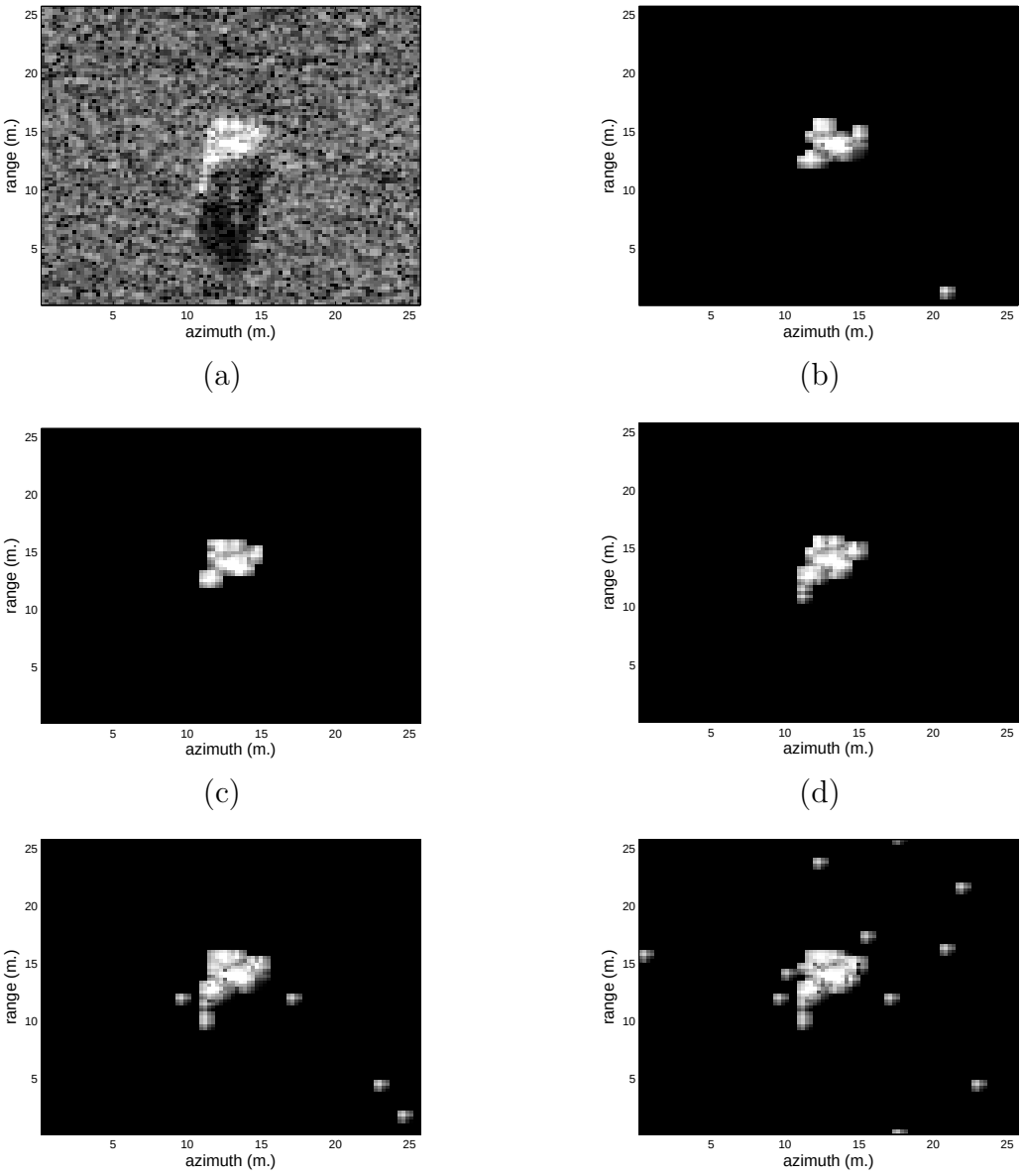

Figure 3.5: The effect of the sparsity parameter, K on image reconstructions by the proposed EMMP technique is illustrated. A military target image from MSTAR database is used for the trials. Only 40% of the Nyquist rate data is used for the reconstructions by the proposed technique. (a) Original image, (b) $K = 30$, (c) $K = 40$, (d) $K = 50$, (e) $K = 70$, and (f) $K = 80$.

close to the actual sparsity level of the target (which is approximately 50), reconstructions provide better results. For K beyond the actual sparsity of the target, it results increased noise in the reconstructed images. Quantitative metrics also support these observations. Table 3.2 illustrates the quantitative image reconstruction metrics for different K values. Again the best results are obtained for the reconstructions with K values around the actual sparsity of the target.

Table 3.2: Effect of sparsity parameter on image reconstruction quality metrics. A military target image from MSTAR database is used for the trials. Only 40% of the raw data is used for the reconstructions by the proposed technique.

K	**MSE**	**TBR**	**H**
30	5.010^{-3}	74.8	0.32
40	2.710^{-3}	∞	0.26
50	1.910^{-3}	∞	0.32
60	2.610^{-3}	65.1	0.46
70	2.510^{-3}	66.5	0.49
80	2.310^{-3}	60.2	0.60

3.4 Comparison of Sparse SAR Image Reconstruction Performances of the Techniques Based on EMMP and Non-Linear Conjugate Gradient Descent Algorithms

In this section, MSTAR images reconstructed by the technique based on non-linear conjugate gradient descent algorithm and presented in Section 2.4.2 are reconstructed by the technique based on EMMP algorithm for comparison purposes. The original MSTAR target images, the synthetic motion error induced images both reconstructed by PFA, the images reconstructed by PFA and autofocused by PGA, and the images reconstructed by the technique based on non-linear

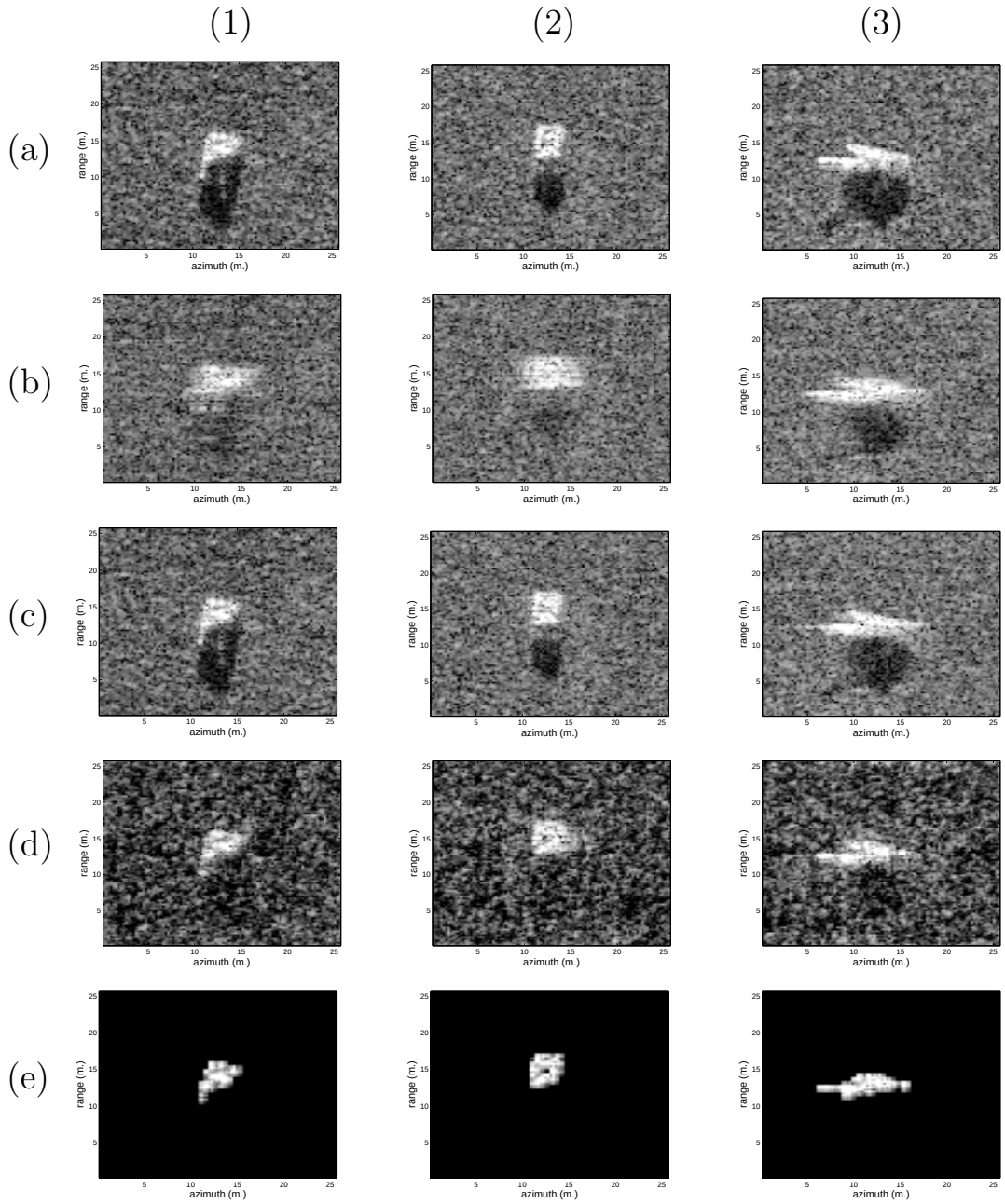

Figure 3.6: Three target images of MSTAR database that are used in the trials. Row (a) gives the original images reconstructed by PFA. Row (b) presents the images with inserted phase error and reconstructed by PFA. Row (c) gives the images reconstructed PFA and autofocused by PGA. Row (d) gives the images reconstructed by CS-PE-TV technique. Row (e) shows the images reconstructed and autofocused by the proposed technique based on EMMP algorithm.

conjugate gradient descent algorithm are again given in the rows (a), (b), (c), and (d) of Figure 3.6 as a benchmark. Reconstructions obtained by the EMMP algorithm for the same target scene are shown in row (e) of Figure 3.6. Note that, only 40% of the Nyquist sampled raw data is used in these reconstructions. Compared to the non-linear conjugate gradient descent algorithm reconstructions given in row (d) of Figure 3.6, reconstructions provided by the EMMP algorithm are of similar. Also, it is observed that the EMMP algorithm provide an effective autofocusing on the reconstructions. Compared to the non-linear conjugate gradient descent algorithm, the advantage of the EMMP algorithm is its computational efficieny and significantly more suppressed speckle noise.

While suppressing all speckle noise effects, the technique based on the EMMP algorithm also removes shadows of targets in the imaged scene. Shadow information in SAR images is valuable and can be used in image classification applications. The technique based on the non-linear conjugate gradient descent algorithm also suppresses shadows. Generally CS based SAR image reconstruction techniques construct only target features but lost shadow data. Retaining shadows in SAR images while reconstructing them by CS techniques has a big impact and will be investigated as a future work. Multichannel autofocus [16, 19] and filtered variation [80] methods seem two potential techniques to solve shadow problem in CS SAR image reconstruction.

The performance metrics defined in Section 2.4.2 are given in Table 2.2 for MSTAR images reconstructed by the technique based on non-linear conjugate gradient descent algorithm. For comparison, same metrics are given in Table 3.3 for MSTAR images reconstructed by the EMMP algorithm. The metrics given in Table 2.2 for PGA and CS-PE-TV reconstructions are repeated in Table 3.3 for reference. For the MSE metric, EMMP algorithm gives a better result than the result of the non-linear conjugate gradient descent algorithm, for target (1). But for other two targets, the results of the non-linear conjugate gradient descent algorithm are better. In terms of the MSE, it is observed that there is no significant quantitative difference between the reconstructions of these algorithms. However, in terms of the TBR and Entropy metrics, the EMMP algorithm provides significantly better reconstructions. Almost total removal of

the speckle noise provides the edge for the EMMP algorithm over the non-linear conjugate gradient descent algorithm. To achieve improved performance levels with respect to the TBR and Entropy metrics with the reconstructions of the non-linear conjugate gradient descent algorithm, a post-processing step designed to suppress the speckle noise can be incorporated to the processing chain. Compared to the non-linear conjugate gradient descent algorithm, the main advantage of the EMMP algorithm is its computational efficiency. An MSTAR reconstruction with the non-linear conjugate gradient descent algorithm takes about 20 hours while the same reconstruction with the EMMP algorithm takes only 3-5 minutes.

Table 3.3: Comparison of performance metrics for the imagery reconstructed by techniques PFA-PGA, CS-PE-TV, and EMMP.

		MSE	**TBR**	**Entropy**
Target 1	**PFA-PGA**	$\mathbf{2.5.10^{-4}}$	29.55	2.50
	CS-PE-TV	$3.6.10^{-3}$	31.59	2.42
	EMMP	$1.9.10^{-3}$	∞	**0.32**
Target 2	**PFA-PGA**	$\mathbf{1.9.10^{-3}}$	27.08	2.95
	CS-PE-TV	$4.5.10^{-3}$	28.41	2.94
	EMMP	$5.4.10^{-3}$	∞	**0.33**
Target 3	**PFA-PGA**	$\mathbf{9.3.10^{-4}}$	26.23	2.80
	CS-PE-TV	$7.2.10^{-3}$	30.23	2.42
	EMMP	$9.6.10^{-3}$	∞	**0.41**

In our SAR imaging techniques detailed in this chapter and the previous chapter, targets are considered as having reflectivity centers on the grid points. Specifically, the measurement matrix, relating measurements to unknown reflectivities, is formed by basis vectors corresponding to on-grid reflectivity centers. The technique with EMMP algorithm presented in this chapter has a side benefit by easily taking into account the off-grid targets case. In the technique using

EMMP algorithm, the measurement matrix could cover the basis vectors corresponding to off-grid points. It perturbs on-grid basis vectors to match off-grid reflectivity responses whose details are given in the next chapter.

Chapter 4

Off-Grid Sparse SAR Image Reconstruction Based on EMMP Algorithm

In Chapter 4, we introduced a robust and efficient SAR image reconstruction technique based on EMMP algorithm. The proposed reconstruction technique provides accurate reconstructions of sparse target scenes. However, it is implicitly assumed that the targets on the scene are located on a discrete range and cross-range grid. Since, this is not a guaranteed condition in practice, it is important to investigate the performance of the proposed technique when targets can be located arbitrarily, which is called as the off-grid target reconstruction problem. In this chapter, by using a recently proposed perturbation technique, the EMMP based reconstruction algorithm is adapted to the case of off-grid targets. In the proposed approach, basis vectors corresponding to on-grid point reflectors are perturbed to adapt to the positions of the off-grid targets.

The received SAR signal at contiguous positions on the flight path which are called as "slow time samples" is discretized by an A/D converter providing "fast time samples". Hence, slow and fast time samples constitute two-dimensional

raw SAR data. By using the received signal on a discrete grid, classical SAR image formation processes provide SAR images with each pixel corresponding only on-grid reflectivity centers. But reflectivity centers of targets generally are not located at exactly on-grid points as illustrated by Figure 4.1. When standard SAR image reconstruction techniques are used, presence of off-grid targets only cause sampling of the point response function of the reconstruction system at a shifted grid. Thus, off-grid target reconstruction does not cause any significant loss in the performance. However, compressed sensing techniques are typically not robust to off-grid targets. For instance, the case shown in Figure 4.1 might cause a reconstruction where pixels far from the target location have significant amplitudes in the reconstructed image. Therefore, unlike classical SAR reconstruction, CS

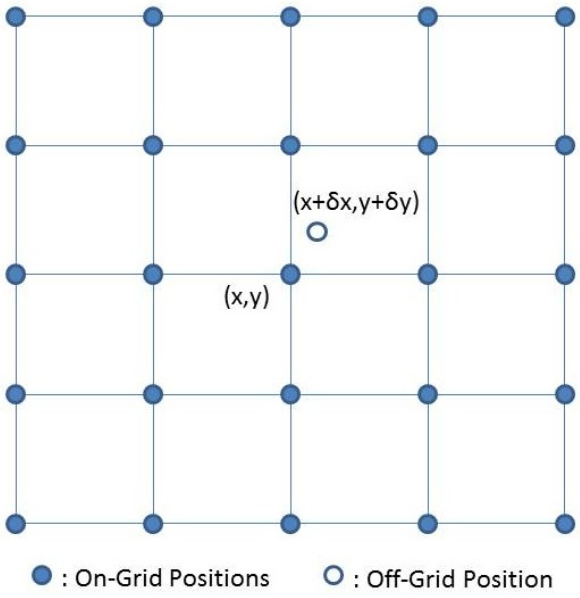

Figure 4.1: Off-grid and on-grid points on a discrete grid.

SAR techniques suffer unacceptable degradation in image quality in the presence of off-grid reflectors. This problem is addressed in recent works on CS SAR image reconstruction [81]. Also, a similar approach including iterative refinement of the dictionary elements is proposed for the problem of parameter estimation for signals characterized for the problem of parametrized functions [82].

In EMMP-SAR imaging technique described in the previous chapter, the measurement matrix, relating measurements to unknown reflectivities, is formed by

basis vectors corresponding to on-grid reflectors. To take into account off-grid case in EMMP-SAR technique, the measurement matrix should cover the basis vectors corresponding to off-grid points. The proposed technique perturbs on-grid basis vectors to match off-grid reflector responses.

In the proposed technique, the target is modeled as containing multiple reflectivity points which can be located on off-grid points. The proposed technique aims to find the off-grid reflectivity point estimates of a target. If there exist closely located multiple targets in the imaged scene, the proposed technique can be applied to all targets iteratively.

4.1 Proposed Off-Grid Sparse SAR Image Reconstruction Technique Based on EMMP Algorithm

CS based optimizations aim to obtain the most sparse signal representation, which corresponds to l_0 norm minimization [32]. But the application of l_0 norm minimization generally is not feasible, because it requires combinatoric search which results prohibitive computational load. Instead, CS optimizations are formulated as l_1 norm minimizations, as in BPDN (Eq. 2.9) and LASSO (Eq. 2.10) formulations whose solutions require less computational loads. In addition, the solutions obtained by l_0 and l_1 norm minimizations are proved to be equivalent if α is sparse and matrix A holds RIP [43].

Contrary to BPDN and LASSO formulations, the EMMP approach provides a near optimal solution to the l_0 norm problem of Eqs. 3.2 which is re-written here,

$$\min_{\alpha} \ \|\mathbf{y} - \mathbf{A}\alpha\|_2 \quad \textit{such that} \quad \|\alpha\|_0 \ \leq \ K, \tag{4.1}$$

where K is the sparsity level of the signal. Similar to τ parameter in LASSO formulation, K can be estimated for man-made targets based on the area of these targets in the scene. The basics of EMMP algorithm are detailed in Section 3.1

Find On-Grid Reflectors
run EMMP with sparsity level K
Find Off-Grid Reflectors
for every point reflector ($i = 1 \dots K$)
perturb $\mathbf{A_i}$
form new dictionary matrix $\mathbf{A_{ip}}$
run EMMP with $\mathbf{A_{ip}}$ and sparsity level 1
find i^{th} off-grid point
end for loop
Output: Off-grid points

Figure 4.2: The proposed SAR-EMMP algorithm

The proposed perturbation technique based on the EMMP algorithm is summarized in Figure 4.1. First it finds the on-grid point reflectors by calling the EMMP algorithm. The sparsity level, K is adjusted according to the target to be imaged. The result of the first run of the EMMP algorithm is the on-grid target position estimates. Together with estimated on-grid points, the corresponding basis vectors are also found as given in Eq. 3.4. In order to adjust for actual reflectivity centers which can be located on off-grid points, the basis vectors, $\mathbf{A}_i$'s, are perturbed around the neighborhood of the estimated on-grid point. The perturbation is handled by constructing a finer grid around the estimated on-grid point as illustrated by Figure 4.3. In computer graphics area, adaptive spatial subdivision techniques similar to finer grid construction have been used widely for ray tracing, object collision, etc. [83]. These finer grid points generate basis vectors forming a new dictionary matrix. Therefore, for every on-grid position, a new dictionary matrix $\mathbf{A}_{ip}$ is formed from the small set of perturbed basis vectors $\mathbf{A}_{ip_j}$. Then, the EMMP algorithm is run with this new dictionary matrix, $\mathbf{A}_{ip}$ and with the sparsity level set to 1. This time the algorithm provides estimates on a finer grid for the off-grid point around the on-grid point i. These steps are repeated for all on-grid points resulting all the corresponding off-grid point estimates on a finer grid. If the resulted resolution is considered inadequate, then the steps of the algorithm can be repeated hierarchically for even finer grids resulting higher resolutions for the off-grid points.

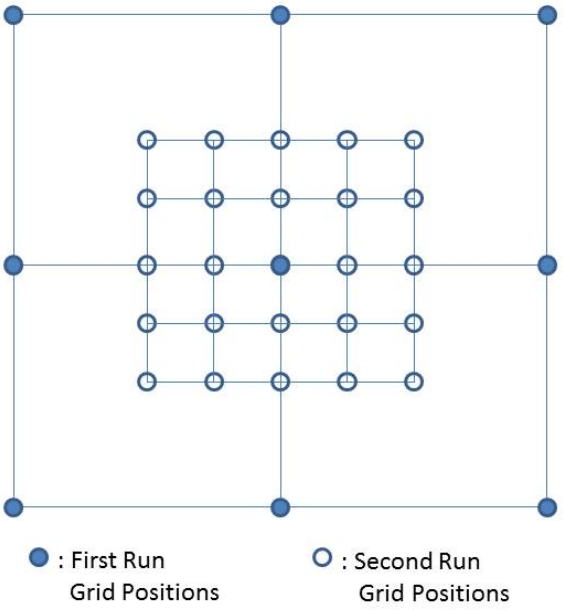

Figure 4.3: Grid points for the reconstruction of the basis vectors. For the first run of the EMMP algorithm the points with full circles are used to reconstruct the basis vectors. The first run gives the on-grid point estimates. Around that point, resolution is increased by constructing a finer grid. Hence, for the second run of the EMMP algorithm the points with empty circles are used to reconstruct the basis vectors.

4.2 Simulations

A synthetically generated SAR data is used to illustrate the performance of the proposed technique. The measurement data is undersampled randomly by the method explained in [76], so only 40% of the original raw data is used in the reconstruction by the proposed technique. The identity matrix is used as the sparsity transform because the image domain is sparse for the synthetic data. The azimuth and range coordinates of the off-grid target reflectivity centers are given in the Actual Coordinates column of Table 4.1.

Table 4.1: The actual and resulting coordinates of the off-grid reflectivity centers.

Point	**Actual Coordinates (m)**		**Output Coordinates (m)**	
No	**Azimuth**	**Range**	**Azimuth**	**Range**
1	0.342	0.114	0.3	0.1
2	2.133	2.215	2.1	2.2
3	−2.267	2.283	−2.3	2.3
4	2.221	−2.119	2.2	−2.1
5	−2.313	−2.225	−2.3	−2.2

The image reconstructed by the classical PFA (Polar Format Algorithm) [7] is given in Figure 4.4. Due to off-grid target points, the image is blurred and the energy of the off-grid points spreads to the neighboring on-grid points.

For comparison, the image reconstructed by the technique using Non-Linear Conjugate Gradient Descent algorithm and detailed in the Chapter 2 is given in Figure 4.5. Similar to PFA reconstruction, the image is again blurred due to the energy spread of the off-grid points to the neighboring on-grid points. This is an expected result because the measurement matrix used in the formulation contains basis vectors corresponding only the on-grid reflectivity points.

The image given in Figure 4.6 is reconstructed by the technique using EMMP algorithm and detailed in the previous chapter with sparsity parameter $K = 5$. The image presents only the neighboring on-grid points with reduced energy. Reconstructing the image by the technique of the previous chapter with different

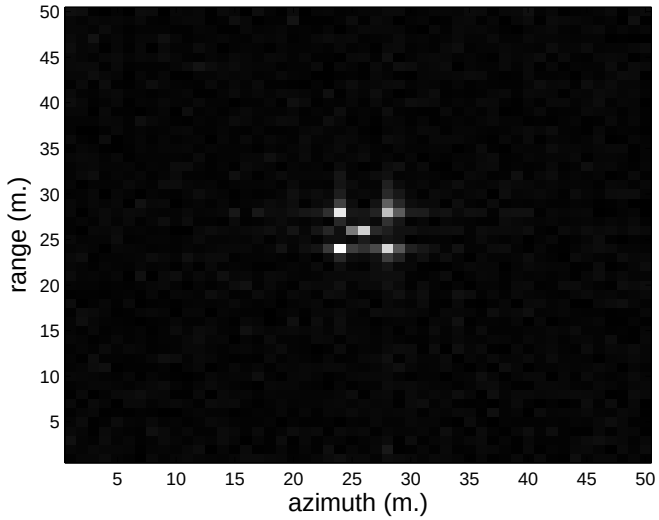

Figure 4.4: The image reconstructed by PFA. The pixel resolution is 1 m. in both azimuth and range directions.

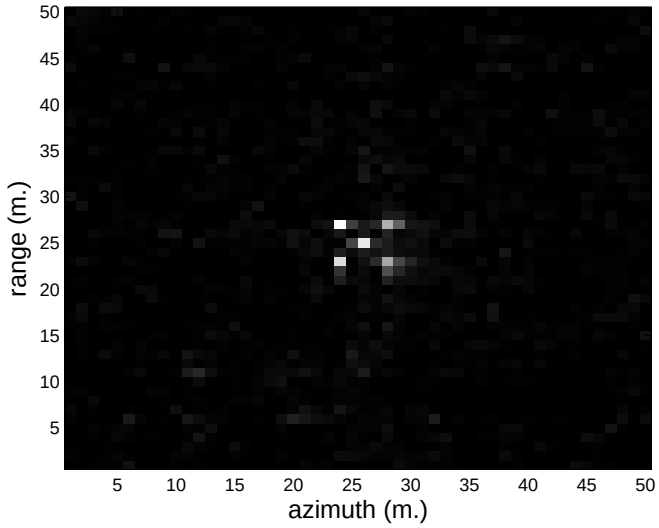

Figure 4.5: The image reconstructed by the technique using Non-Linear Conjugate Gradient Descent algorithm which is detailed in the Chapter 2. The pixel resolution is 1 m. in both azimuth and range directions.

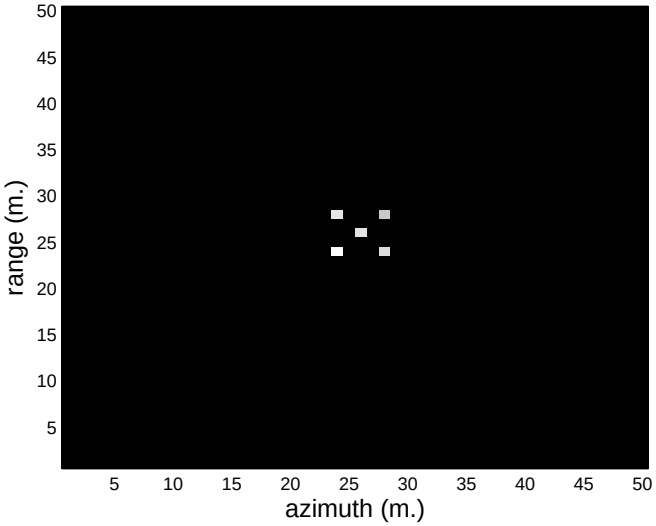

Figure 4.6: The image reconstructed by EMMP algorithm with sparsity parameter $K = 5$. The pixel resolution is 1 m. in both azimuth and range directions.

K parameters reveals the effects of the off-grid points. The effect of K parameter on image reconstruction quality is analyzed in [78]. Figure 4.7 displays an output image reconstructed by the technique of the previous chapter with $K = 10$. The effects of the off-grid points are clearly seen as their energy disperses to the neighboring pixels.

The proposed technique based on the iterative application of EMMP algorithm to find the off-grid target points is applied to the synthetically generated data. The technique is applied to the data just one iteration which results finer grid resolution around the on-grid locations. One iteration of the technique resulted accuracy level set to the tenths digit. The results are listed in the Output Coordinates column of Table 4.1. The resulted coordinates obtained by the proposed technique match with the actual coordinates up to tenths digit which proves the efficient application of the method. Because grids become finer in every application and they determine the resolution of the reconstruction, so higher resolutions can be obtained by repeated application of the technique to the off-grid points. But this method has a resolution limit reached when the base vectors created by finer grids do not result a residual change greater than ϵ in EMMP algorithm. The relation between the achievable resolution level of the reconstruction and

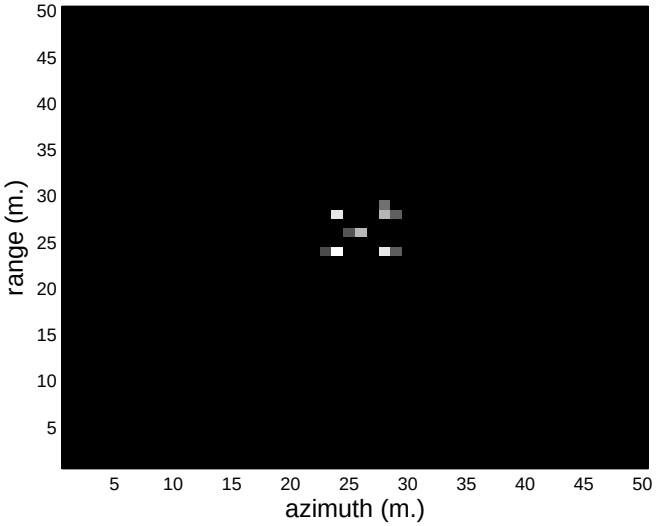

Figure 4.7: The image reconstructed by EMMP algorithm with sparsity parameter $K = 10$. The pixel resolution is 1 m. in both azimuth and range directions.

the parameter ϵ, which is related to the noise level of the measured data will be investigated thoroughly in a future work.

The perturbation of basis vectors around the neighborhood of the on-grid points results the detection of off-grid points with high precision. The EMMP algorithm is a fast one compared to other alternative CS reconstruction techniques like conjugate gradient methods. The proposed technique calls the EMMP algorithm inside a for loop with small sized A_{ip} matrix just for the neighboring off-grid points and with sparsity level $K = 1$, which results computationally efficient and fast method.

Chapter 5

Conclusions and Future Work

SAR imaging of man-made targets has found many applications. Platform motion caused phase errors are the main cause of SAR image degradations. Autofocus algorithms are applied to SAR images to compensate phase error effects. Sparsity found in man-made target SAR images brings the application of CS techniques to SAR image reconstruction. CS techniques can be applied to sparse SAR image reconstruction to gain practical advantages such as reduced memory requirement and A/D converter rates.

This thesis focuses on the main problems of sparse SAR image reconstruction. Especially, the platform motion caused phase errors and their compensation are examined in detail. New and robust techniques are proposed to reconstruct and autofocus SAR images simultaneously. Combining SAR image reconstruction and phase error compensation processes into a single step is an advantage over the classical image reconstruction techniques. To take advantage of applying CS framework and so to reduce the rate of A/D conversion and memory requirement, a specific under sampling pattern is also introduced. In addition to techniques dealing with phase error compensation, a new method is also proposed for off-grid SAR image reconstruction.

In Chapter 2, a compressive sensing framework is proposed for simultaneous motion compensation and image reconstruction for SAR data obtained at a

fraction of Nyquist rate of sampling. Under-sampling is performed by using reduced rate A/D converters which also decrease the required memory size and the bandwidth of the data link. To improve performance, a total variation penalty on the reconstructed image is also incorporated into the proposed optimization technique. Non-Linear Conjugate Gradient Descent algorithm is used to obtain the optimum solution of the cost function. Detailed investigation of the reconstructions of both synthetic and real data sets demonstrates that, under well recognized performance metrics, the proposed CS-PE-TV technique improves performance over the common PFA-PGA technique and other alternative CS based techniques. Research on the more efficient optimization of the proposed CS-PE-TV cost function is expected to reduce the computational requirements of the proposed technique and increase its applicability.

In Chapter 3, autofocused SAR image reconstruction is modeled again as a CS problem but it is now solved by using EMMP algorithm. The proposed EMMP based autofocused SAR reconstruction technique provides efficient reconstructions of SAR images even under severe phase errors. Since, it requires only a fraction of the Nyquist rate samples, the proposed technique also relaxes the requirements on the SAR hardware. Unlike alternative l_1 norm minimization based approaches, the proposed technique provides near optimal solution to the desired l_0 norm minimization problem efficiently by a sequential search procedure in 1-dimensional search spaces. Moreover, EMMP algorithm converges faster compared to Non-Linear Conjugate Gradient Descent algorithm for CS reconstructions while providing comparable quality outputs. Comparison with PFA-PGA technique over synthetic and real data sets with man-made targets shows that the proposed technique provides comparable or more improved reconstructions. In addition, since EMMP reconstructions are highly localized with significantly suppressed speckle, it enables improved target classification. Application of CS to SAR image reconstruction provides to emphasize the desired features of the target by carefully adjusting the parameters in the cost function. This characteristic can have impacts in SAR image classification area. Controlling target features by cost function parameters and hence obtain the dominant target features for classification can be examined deeply in a future work.

Our proposed techniques based on non-linear conjugate gradient descent and EMMP algorithms retain target features in SAR images while suppressing shadows of targets in the imaged scene. This is a general characteristic of CS based SAR image reconstruction techniques. But shadow information in SAR images is valuable and can be used in image classification applications. Therefore, retaining shadows in SAR image reconstruction by CS techniques has a big impact and will be investigated as a future work.

For targets with off-grid reflectivity centers, an EMMP based technique is proposed providing efficient SAR image reconstruction in Chapter 4. This technique is the same as the technique described in Chapter 3 with small modifications. Therefore the EMMP algorithm based technique has an advantage of providing reconstruction of SAR images of off-grid targets. The proposed technique is based on the iterative application of the EMMP algorithm to find the off-grid target points. EMMP algorithm provides fast reconstructions due to the faster convergence of the EMMP algorithm compared to alternative gradient descent based optimization techniques for CS reconstructions. Numerical experiments on the synthetic data set show that the proposed technique provides off-grid coordinates for reconstruction with high precision. Repeated application of the technique to the off-grid points determines the resolution of the off-grid reconstruction. The resolution limit is reached when the base vectors created by finer grids do not result a residual change greater than ϵ. The relation between the achievable resolution level of the reconstruction and the parameter ϵ, which is related to the noise level of the measured data will be investigated thoroughly in a future work.

Bibliography

[1] C. Wu, K. Y. Liu, and M. J. Jin, "A modelling and correlation algorithm for spaceborne SAR signals," *IEEE Transactions on Aerospace and Electronic Systems*, vol. AES-18, no. 5, pp. 563–574, 1982.

[2] B. C. Barber, "Theory of digital imaging from orbital synthetic aperture radar," *International Journal of Remote Sensing*, vol. 6, no. 7, pp. 1009–1057, 1985.

[3] A. M. Smith, "A new approach to range doppler SAR processing," *International Journal of Remote Sensing*, vol. 12, no. 2, pp. 235–251, 1991.

[4] R. K. Raney, H. Runge, R. Bamler, I. G. Cumming, and F. H. Wong, "Precision SAR processing using chirp scaling," *IEEE Transactions on Geoscience and Remote Sensing*, vol. 32, no. 4, pp. 786–799, 1994.

[5] C. Cafforio, C. Prati, and F. Roca, "SAR data focusing using seismic migration techniques," *IEEE Transactions on Aerospace and Electronic Systems*, vol. 27, no. 2, pp. 194–207, 1991.

[6] W. G. Carrara, R. S. Goodman, and R. M. Majewski, *Spotlight Synthetic Aperture Radar, Signal Processing Algorithms*. Artech House Inc., 1995.

[7] D. C. Munson Jr, J. C. O'Brien, and W. K. Jenkins, "A tomographic formulation of spotlight-mode synthetic aperture radar," *Proc. IEEE*, vol. 71, no. 8, pp. 971–925, 1983.

[8] M. D. Desai and W. K. Jenkins, "Convolution backprojection image reconstruction for spotlight mode synthetic aperture radar," *IEEE Transactions on Image Processing*, vol. 1, pp. 505–517, October 1992.

[9] M. Çetin and W. C. Karl, "Feature-enhanced synthetic aperture radar image formation based on nonquadratic regularization," *IEEE Transactions on Image Processing*, vol. 10, pp. 623–631, April 2001.

[10] V. M. Patel, G. R. Glenn, D. M. Healy, and R. Chellappa, "Compressed synthetic aperture radar," *IEEE Journal of Selected Topics in Signal Processing*, vol. 4, pp. 244–254, April 2010.

[11] C. V. Jakowatz Jr, D. E. Wahl, P. H. Eichel, D. C. Ghiglia, and P. A. Thompson, *Spotlight-Mode Synthetic Aperture Radar: A Signal Processing Approach*. Springer Science+Business Media, LLC, 1996.

[12] C. E. Mancill and J. M. Swiger, "A mapdrift autofocus technique for correcting higher order SAR phase errors," in 27^{th} *Annual Tri-Service Radar Symposium Record*, pp. 391–400, 1981.

[13] L. Xi, L. Guosui, and J. Ni, "Autofocusing of ISAR images based on entropy minimization," *IEEE Transactions on Aerospace and Electronic Systems*, vol. 35, pp. 1240–1252, October 1999.

[14] C. V. Jakowatz Jr and D. E. Wahl, "Eigenvector method for maximum-likelihood estimation of phase errors in synthetic-aperture-radar imagery," *J. Opt. Soc. Am. A*, vol. 10, pp. 2539–2546, December 1993.

[15] R. L. Morrison, M. N. Do, and D. C. Munson Jr, "SAR image autofocus by sharpness optimization: A theoretical study," *IEEE Transactions on Image Processing*, vol. 16, pp. 2309–2321, September 2007.

[16] R. L. Morrison, M. N. Do, and D. C. Munson Jr, "MCA: A multichannel approach to SAR autofocus," *IEEE Transactions on Image Processing*, vol. 18, pp. 840–853, April 2009.

[17] P. H. Eichel, D. C. Ghiglia, and C. V. Jakowatz, "Speckle processing method for synthetic aperture radar phase correction," *Optics Letters*, vol. 14, pp. 1–3, October 1989.

[18] D. E. Wahl, P. H. Eichel, D. C. Ghiglia, and C. V. Jakowatz, "Phase gradient autofocus - a robust tool for high resolution SAR phase correction," *IEEE Transactions on Aerospace and Electronic Systems*, vol. 30, pp. 827–835, October 1994.

[19] H. J. Cho and D. C. Munson Jr, "Multichannel sar autofocus using multiple low-return constraints," in *IEEE International Conference on Acoustics Speech and Signal Processing*, pp. 1346–1349, 2010.

[20] K. H. Liu and D. C. Munson Jr, "Fourier-domain multichannel autofocus for synthetic aperture radar," *IEEE Transactions on Image Processing*, vol. 20, pp. 3544–3552, December 2011.

[21] K. H. Liu, A. Weisel, and D. C. Munson Jr, "Synthetic aperture radar autofocus via semidefinite relaxation," in *IEEE International Conference on Acoustics Speech and Signal Processing*, pp. 1342–1345, 2010.

[22] K. H. Liu, A. Weisel, and D. C. Munson Jr, "Synthetic aperture radar autofocus based on a bilinear model," *IEEE Transactions on Image Processing*, vol. 21, pp. 2735–2746, May 2012.

[23] R. Baraniuk and P. Steeghs, "Compressive radar imaging," in *IEEE Radar Conference*, pp. 128–133, 2007.

[24] S. Bhattacharya, T. Blumensath, B. Mulgrew, and M. Davies, "Fast encoding of synthetic aperture radar raw data using compressed sensing," in *IEEE/SP* 14^{th} *Workshop on Statistical Signal Processing*, pp. 448–452, 2007.

[25] S. J. Wei, X. L. Zhang, J. Shi, and G. Xiang, "Sparse reconstruction for SAR imaging based on compressed sensing," *Progress In Electromagnetics Research*, vol. 109, pp. 63–81, 2010.

[26] E. van den Berg and M. P. Friedlander, "Probing the Pareto frontier for basis pursuit solutions," *SIAM Journal on Scientific Computing*, vol. 31, pp. 890–912, January 2009.

[27] E. Candès and J. Romberg, "L1 Magic, accessed at june 2013," http://www-stat.stanford.edu/candes/l1magic.

[28] B. D. Rigling, "Use of nonquadratic regularization in fourier imaging," *IEEE Transactions on Aerospace and Electronic Systems*, vol. 45, pp. 250–264, January 2009.

[29] G. O. Önhon and M. Çetin, "Joint sparsity-driven inversion and model error correction for radar imaging," in *IEEE International Conference on Acoustics Speech and Signal Processing*, pp. 1206–1209, 2010.

[30] S. I. Kelly, G. Rilling, M. Davies, and B. Mulgrew, "Iterative image formation using fast (re/back)-projection for spotlight-mode SAR," in *IEEE Radar Conference*, pp. 835–840, 2011.

[31] L. C. Potter, E. Ertin, J. T. Parker, and M. Çetin, "Sparsity and compressed sensing in radar imaging," *Proceedings of the IEEE*, vol. 98, pp. 1006–1020, June 2010.

[32] D. L. Donoho, "Compressed sensing," *IEEE Transactions on Information Theory*, vol. 52, pp. 1289–1306, April 2006.

[33] E. Candès and T. Tao, "Near-optimal signal recovery from random projections: Universal encoding strategies?," *IEEE Transactions on Information Theory*, vol. 52, pp. 5406–5425, December 2006.

[34] S. S. Chen, D. L. Donoho, and M. A. Saunders, "Atomic decomposition by basis pursuit," *SIAM Journal on Scientific Computing*, vol. 20, no. 1, pp. 33–61, 1998.

[35] S. Mallat and Z. Zhang, "Matching pursuits with time-frequency dictionaries," *IEEE Transactions on Signal Processing*, vol. 41, pp. 3397–3415, December 1993.

[36] J. A. Tropp, "Greed is good: Algorithmic results for sparse approximation," *IEEE Transactions on Information Theory*, vol. 50, pp. 2231–2242, October 2004.

[37] J. A. Tropp, "Just relax: Convex programming methods for identifying sparse signals in noise," *IEEE Transactions on Information Theory*, vol. 52, pp. 1030–1051, March 2006.

[38] R. Baraniuk, V. Cevher, M. Duarte, and C. Hedge, "Model-based compressive sensing," *IEEE Transactions on Information Theory*, vol. 56, pp. 1982–2001, April 2010.

[39] J. A. Tropp and A. C. Gilbert, "Signal recovery form random measurements via orthogonal matching pursuit," *IEEE Transactions on Information Theory*, vol. 53, pp. 4655–4666, December 2007.

[40] I. F. Gorodnitsky and B. D. Rao, "Sparse signal reconstruction from limited data using FOCUSS: A re-weighted minimum norm algorithm," *IEEE Transactions on Signal Processing*, vol. 45, pp. 600–616, March 1997.

[41] W. Yin, S. Osher, D. Goldfarb, and J. Darbon, "Bregman iterative algorithms for l_1-minimization with applications to compressed sensing," *SIAM Journal on Imaging Sciences*, vol. 1, pp. 143–168, 2008.

[42] D. L. Donoho and M. Elad, "Optimally sparse representation in general (nonorthogonal) dictionaries via l1 minimization," *The Proc. Nat. Aca. Sci.*, vol. 100, pp. 2197–2202, March 2003.

[43] E. Candès, J. Romberg, and T. Tao, "Stable signal recovery from incomplete and inaccurate measurements," *Communications on Pure and Applied Mathematics*, vol. 59, no. 8, pp. 1207–1223, 2006.

[44] E. Candès, J. Romberg, and T. Tao, "Robust uncertainty principles: Exact signal reconstruction from highly incomplete frequency information," *IEEE Transactions on Information Theory*, vol. 52, pp. 489–509, February 2006.

[45] E. Candès and M. B. Wakin, "An introduction to compressive sampling," *IEEE Signal Processing Magazine*, vol. 25, pp. 21–30, March 2008.

[46] M. Herman and T. Strohmer, "Compressed sensing radar," in *IEEE Radar Conference*, pp. 1–6, May 2008.

[47] M. Herman and T. Strohmer, "High resolution radar via compressed sensing," *IEEE Transactions on Signal Processing*, vol. 57, pp. 2275–2284, June 2009.

[48] G. E. Smith, T. Diethe, Z. Hussain, J. S. Taylor, and D. R. Hardoon, "Compressed sampling for pulse doppler radar," in *IEEE Radar Conference*, pp. 887–892, May 2010.

[49] Q. Huang, L. Qu, B. Wu, and G. Fang, "UWB through-wall imaging based on compressive sensing," *IEEE Transactions on Geoscience and Remote Sensing*, vol. 48, pp. 1408–1415, March 2010.

[50] C. Oliver and S. Quegan, *Understanding Synthetic Aperture Radar Images*. SciTech Publishing, 2004.

[51] G. Rilling, M. Davies, and B. Mulgrew, "Compressed sensing based compression of SAR raw data," in *SPARS'09 - Signal Processing with Adaptive Sparse Structured Representations*, March 2009.

[52] R. Baraniuk, "Compressive sensing," *IEEE Signal Processing Magazine*, vol. 24, pp. 118–121, July 2007.

[53] M. Lustig, D. Donoho, and D. M. Pauly, "Sparse MRI: The application of compressed sensing for rapid MR imaging," *Magnetic Resonance in Medicine*, vol. 58, pp. 1182–1195, December 2007.

[54] G. Hennenfent and F. J. Herrmann, "Simply denoise: Wavefield reconstruction via jittered undersampling," *Geophysics*, vol. 73, pp. 19–28, June 2008.

[55] M. Mishali, Y. C. Eldar, O. Dounaevsky, and E. Shoshan, "Xampling: Analog to digital at sub-Nyquist rates," *IET Circuits, Devices & Systems*, vol. 5, pp. 8–20, January 2011.

[56] R. Tibshirani, "Regression shrinkage and selection via the Lasso," *J. Roy. Statist. Soc. Ser. B.*, vol. 58, pp. 267–288, 1996.

[57] W. Boyd and L. Vandenberghe, *Convex Optimization*. Cambridge University Press, 2004.

[58] E. Candès and J. Romberg, "Practical signal recovery from random projections," in *Computational Imaging III : Proc. SPIE International Symposium on Electronic Imaging*, pp. 76–86, 2005.

[59] L. I. Rudin, S. Osher, and E. Fatemi, "Nonlinear total variation based noise removal algorithms," *Physica D*, vol. 60, pp. 259–268, 1992.

[60] M. M. Bronstein, A. M. Bronstein, M. Zibulevsky, and H. Azhari, "Reconstruction in diffraction ultrasound tomography using nonuniform FFT," *IEEE Transactions on Medical Imaging*, vol. 21, no. 11, pp. 1395–1401, 2002.

[61] K. T. Block, M. Uecker, and J. Frahm, "Undersampled radial MRI with multiple coils. Iterative image reconstruction using a total variation constraint," *Magnetic Resonance in Medicine*, vol. 57, pp. 1086–1098, 2007.

[62] D. P. Bertsekas, *Nonlinear Programming*. Athena Scientific, 1995.

[63] J. F. Cai, S. Osher, and Z. Shen, "Split Bregman methods and frame based image restoration," *SIAM Multiscale Modeling and Simulation*, vol. 8, no. 2, pp. 337–369, 2009.

[64] J. F. Cai, S. Osher, and Z. Shen, "Linearized Bregman iterations for compressed sensing," *Mathematics of Computation*, vol. 78, no. 267, pp. 1515–1536, 2009.

[65] J. F. Cai, S. Osher, and Z. Shen, "Linearized Bregman iterations for frame-based image deblurring," *SIAM Journal on Imaging Sciences*, vol. 2, no. 1, pp. 226–252, 2009.

[66] The MathWorks, Inc., Natick, MA, USA.

[67] K. Goto and R. A. V. de Geijn, "Anatomy of high-performance matrix multiplication," *ACM Transactions on Mathematical Software*, vol. 34, May 2008.

[68] J. A. Gunnels, G. M. Henry, and R. A. V. de Geijn, "A family of high-performance matrix multiplication algorithms," in *ICCS 2001, Lecture Notes in Computer Science*, vol. 2073, pp. 51–60, 2001.

[69] https:///www.sdms.afrl.af.mil. The Sensor Data Management System MSTAR public data.

[70] M. Çetin, *Feature-Enhanced Synthetic Aperture Radar Imaging*. PhD thesis, College of Engineering, Boston University, Boston, 2001.

[71] S. Samadi, M. Çetin, and M. A. Masnadi-Shirazi, "Sparse representation based synthetic aperture radar imaging," *IET Radar, Sonar and Navigation*, vol. 5, pp. 182–193, February 2011.

[72] M. Çetin, W. C. Karl, and D. A. C. non, "Feature enhancement and ATR performance using nonquadratic optimization-based SAR imaging," *IEEE Transactions on Aerospace and Electronic Systems*, vol. 39, pp. 1375–1395, October 2003.

[73] A. C. Gürbüz, M. Pilancı, and O. Arıkan, "Expectation maximization based matching pursuit," in *IEEE International Conference on Acoustics Speech and Signal Processing*, March 2012.

[74] S. Uğur, A. C. Gürbüz, and O. Arıkan, "SAR image reconstruction by EMMP algorithm," in *IEEE* 20^{th} *Conference on Signal Processing and Communication Applications*, (Antalya, Turkey), April 2012.

[75] S. Uğur, A. C. Gürbüz, and O. Arıkan, "Autofocused sparse SAR image reconstruction by EMMP algorithm," in 1^{st} *International Workshop on Compressed Sensing Applied to Radar*, (Bonn, Germany), May 2012.

[76] S. Uğur and O. Arıkan, "SAR image reconstruction and autofocus by compressed sensing," *Digital Signal Processing*, vol. 22, pp. 923–932, December 2012.

[77] S. I. Kelly, G. Rilling, M. Davies, and B. Mulgrew, "Iterative image formation using fast (re/back)-projection for spotlight-mode SAR," in *IEEE Radar Conference*, pp. 835–840, May 2011.

[78] S. Uğur, A. C. Gürbüz, and O. Arıkan, "Autofocused sparse SAR image reconstruction by EMMP algorithm," submitted to " *IEEE Transactions on Aerospace and Electronic Systems*".

[79] A. Dempster, N. Laird, and D. Rubin, "Maximum likelihood from incomplete data via the EM algorithm," *J. Roy. Statist. Soc. Ser. B.*, vol. 39, no. 1, pp. 1–38, 1977.

[80] K. Köse, V. Cevher, and A. E. Çetin, "Filtered variation method for denoising and sparse signal processing," in *IEEE International Conference on Acoustics Speech and Signal Processing*, pp. 3329–3332, 2012.

[81] A. Fannjiang and H. C. Tseng, "Compressive radar with off-grid and extended targets," arXiv:1209.6399.

[82] C. D. Austin, J. N. Ash, and R. L. Moses, "Parameter estimation using sparse reconstruction with dynamic dictionaries," in *IEEE International Conference on Acoustics Speech and Signal Processing*, May 2011.

[83] P. Ning and J. Bloomenthal, "An evaluation of implicit surface tilers," *IEEE Computer Graphics and Applications*, vol. 13, pp. 33–41, November 1993.

Appendix A

Gradient of the Cost Function

The technique which simultaneously reconstructs and autofocuses sparse SAR images is detailed in Chapter 2. The cost function (Eq. 2.20) in the proposed technique is solved numerically by the non-linear conjugate gradient descent algorithm with backtracking line search [53, 62]. In the optimization iterations of the algortihm, the gradient of the cost function is to be computed. This appendix presents the gradient of the cost function in Eq. 2.20.

The first term of the cost function in Eq. 2.20 includes absolute values. The absolute value is not a smooth function so it is approximated by,

$$|x| = \sqrt{xx^* + \epsilon}, \tag{A.1}$$

where ϵ is a small positive smoothing parameter. By using this approximation, the gradient of the first term in the cost function given in Eq. 2.20 becomes,

$$\nabla \|\mathbf{\Psi}^H \mathbf{x}\|_1 = \mathbf{\Psi}\ \mathbf{W}_1^{-1} \mathbf{\Psi}^H\ \mathbf{x}, \tag{A.2}$$

where $\mathbf{W}_1$ is a diagonal matrix with corresponding elements,

$$w_i = \sqrt{|(\mathbf{\Psi}^H \mathbf{x})_i|^2 + \epsilon_1}. \tag{A.3}$$

Since the total variation is also a non-smooth function, the following approximation is used,

$$TV(\mathbf{x}) = \sum_{i,j} \sqrt{|\nabla_i x|_{i,j}^2 + |\nabla_j x|_{i,j}^2 + \mu}, \tag{A.4}$$

where μ is a small positive smoothing parameter. With this approximation, the gradient of the total variation part of the cost function is given by [60],

$$\nabla\, TV(\mathbf{x}) \;=\; I_{i,j} - I_{i+1,j} + J_{i,j} - J_{i,j+1}, \tag{A.5}$$

where

$$I_{i,j} \;=\; \frac{(\nabla_i x)_{i,j}}{\sqrt{(\nabla_i x)^2_{i,j} + (\nabla_j x)^2_{i,j} + \mu}}, \tag{A.6}$$

$$J_{i,j} \;=\; \frac{(\nabla_j x)_{i,j}}{\sqrt{(\nabla_i x)^2_{i,j} + (\nabla_j x)^2_{i,j} + \mu}}. \tag{A.7}$$

The third term in the cost function is re-written below,

$$\|\mathbf{y}_u - \mathbf{\Phi}\ \mathbf{G}_u\mathbf{x}\|_2^2 \;= \mathbf{y}_u^H\mathbf{y}_u + \mathbf{x}^H\mathbf{G}_u^H\mathbf{G}_u\mathbf{x}\ - \mathbf{y}_u^H\mathbf{\Phi}\ \mathbf{G}_u\mathbf{x}\ - \mathbf{x}^H\mathbf{G}_u^H\mathbf{\Phi}^H\mathbf{y}_u. \tag{A.8}$$

The last two terms of the above equation can be expanded as,

$$\begin{aligned}\|\mathbf{y}_u - \mathbf{\Phi}\ \mathbf{G}_u\mathbf{x}\|_2^2 \;=& \mathbf{y}_u^H\mathbf{y}_u + \mathbf{x}^H\mathbf{G}_u^H\mathbf{G}_u\mathbf{x} \\ &- \sum_{i=1}^{N} e^{j\phi_i}\mathbf{y}_{ui}^H\mathbf{G}_{ui}\mathbf{x}\ - \sum_{i=1}^{N} e^{-j\phi_i}\mathbf{x}^H\mathbf{G}_{ui}^H\mathbf{y}_{ui}.\end{aligned} \tag{A.9}$$

Putting the relation $\phi_i \;=\; \angle\,(\mathbf{x}^H\ \mathbf{G}_{ui}^H\ \mathbf{y}_{ui})$ which is obtained by Eq. 2.14 into the above equation,

$$\|\mathbf{y}_u - \mathbf{\Phi}\ \mathbf{G}_u\mathbf{x}\|_2^2 \;= \mathbf{y}_u^H\mathbf{y}_u + \mathbf{x}^H\mathbf{G}_u^H\mathbf{G}_u\mathbf{x}\ - 2\sum_{i=1}^{N}\ |\mathbf{y}_{ui}^H\mathbf{G}_{ui}\mathbf{x}|. \tag{A.10}$$

By using the approximation in Eq. A.1, the gradient of the third term of the cost function is given by,

$$\begin{aligned}\nabla\|\mathbf{y}_u - \mathbf{\Phi}\ \mathbf{G}_{ui}\mathbf{x}\|_2^2 \;=& \ 2\ \mathbf{G}_u^H\ \mathbf{G}_u\ \mathbf{x} \\ &- 2\ \sum_{i=1}^{N}\ \frac{\mathbf{y}_{ui}^H\mathbf{G}_{ui}\mathbf{x}}{\sqrt{\mathbf{x}^H\mathbf{G}_{ui}^H\mathbf{y}_{ui}\mathbf{y}_{ui}^H\mathbf{G}_{ui}\mathbf{x} + \epsilon_2}}\ \mathbf{G}_{ui}^H\ \mathbf{y}_{ui}.\end{aligned} \tag{A.11}$$

By combining gradients of all these three terms, the following final expression for the gradient of the cost function is obtained:

$$\begin{aligned}\nabla g(\mathbf{x}) \;=& \ \mathbf{\Psi}\mathbf{W}_1^{-1}\mathbf{\Psi}^H\ \mathbf{x}\ +\ \beta\ (I_{i,j} - I_{i+1,j} + J_{i,j} - J_{i,j+1})\ + \\ &\gamma\ (\ 2\mathbf{G}_u^H\mathbf{G}_u\mathbf{x} - 2\sum_{i=1}^{N}\ \frac{\mathbf{y}_{ui}^H\mathbf{G}_{ui}\mathbf{x}}{\sqrt{\mathbf{x}^H\mathbf{G}_{ui}^H\mathbf{y}_{ui}\mathbf{y}_{ui}^H\mathbf{G}_{ui}\mathbf{x} + \epsilon_2}}\ \mathbf{G}_{ui}^H\mathbf{y}_{ui}).\end{aligned} \tag{A.12}$$

Eq. A.12 is the final form of the gradient function required in the optimization iterations of the cost function in Eq. 2.20 by using the non-linear conjugate gradient descent algorithm with backtracking line search.